Astronomy & Astrophysics manuscript no. Darx345
July 1, 2022
© ESO 2022

arXiv:2206.14995v1 [astro-ph.GA] 30 Jun 2022

Doppler boosting effect and flux evolution of superluminal components in QSO 3C345

S.J. Qian[1]

National Astronomical Observatories, Chinese Academy of Sciences, Beijing 100012, China

Compiled by using A&A latex

ABSTRACT

Context. The precessing jet-nozzle scenario previously proposed was applied to interpret the VLBI-measured kinematics of five superluminal components (C4, C5, C9, C10 and C22) and their flux density evolution in blazar 3C345.
Aims. It is shown that in the inner-trajectory sections their kinematic properties, including trajectory, coordinates, core separation and apparent velocity can be well model-simulated by using the scenario with a precession period of 7.30 yr (4.58 yr in the source frame) and a precessing common trajectory, which produces the individual knot-trajectories at their corresponding precession phases.
Methods. Through the model-simulation of their kinematic behavior their bulk Lorentz factor, viewing angle and Doppler factor were derived as functions of time. These anticipatively determined Lorentz /Doppler factors were used to investigate the knots' Doppler-boosting effect and interpret their flux evolution.
Results. It was found that the light-curves of the five superluminal components observed at 15, 22 and 43 GHz were extraordinarily well coincident with their Doppler boosting profiles ($[\delta(t)/\delta_{max}]^{3+\alpha}$, α–spectral index). Additionally, some flux fluctuations on shorter time-scales could be due to variations in knots' intrinsic flux and spectral index.
Conclusions. The close relation between the flux evolution and the Doppler-boosting effect not only firmly validates the precessing jet-nozzle scenario being fully appropriate to explain the kinematic and emission properties of superluminal components in QSO 3C345, but also strongly supports the traditional common point-view: superluminal components are physical entities (shocks or plasmoids) participating relativistic motion toward us with acceleration/deceleration along helical trajectories.

Key words. galaxies: active – galaxies: jets – galaxies: nucleus – galaxies: individual 3C345

1. Introduction

3C345 (z=0.595) is a prototypical quasar emanating emission over the entire electromagnetic spectrum from radio, infrared, optical, UV and X-rays to high-energy γ rays. It is also one of the best-studied blazars (e.g., Biretta et al. 1986, Hardee et al. 1987, Steffen et al. 1996, Unwin et al. 1997, Zensus et al. 1997, Klare 2003, Klare et al. 2005, Lobanov & Roland 2005, Jorstad et al. 2005, 2013, 2017, Qian et al. 1991a, 1996, 2009, Schinzel et al. 2010, Schinzel 2011a, Schinzel et al. 2011b, Homan et al. 2014). Its remarkable and violent variations in all these wavebands and the spectral energy distribution have been extensively monitored and studied, leading to many important results on the emission properties of the source. Studies of the correlation between the variabilities at multi-frequencies (from radio to γ rays) play an important role.
3C345 is a remarkable compact flat-spectrum radio source which was one of the firstly discovered quasars to have a relativistic jet, emanating superluminal components steadily. VLBI-observations have revealed the parsec structure of its jet and monitored the kinematic behavior of its superluminal components ejected from the radio core over a quite long time-interval since ∼1979.
It has been shown that flaring activities of the source in multi-frequencies (from radio to γ-rays) are closely connected with the jet-activity and ejection of superluminal components. In addition, VLBI-monitoring observations have shown that the swing of the knot's ejection position angle and the apparent direction of its relativistic jet could be produced by jet-precession (or jet-nozzle precession) with a precession period of ∼5-10 years. The determination of its jet-nozzle precession may be very important for understanding the kinematics of superluminal components and the properties of the central energy engine in its nucleus.
Since 1991 (Qian et al. 1991a, 2009), we have tried to interpret the VLBI-kinematics of superluminal components in 3C345 in terms of a precessing jet-nozzle scenario. In the recent work (Qian 2022) the kinematics of twenty-seven superluminal components observed during a 38 yr period was explained in detail. It was found that these superluminal knots could be divided into two groups, which were suggestively ejected by their respective precessing jet nozzle. Based on this division the precession period of both nozzles was derived to be 7.3±0.36 yr in the same direction.
Our precessing jet-nozzle scenario proposed to interpret the VLBI-measured kinematics in 3C345 and other blazars has been based on two assumptions:

– (1) jet-nozzle precesses with a certain period and ejects superluminal components and magnetized plasmas at different precession phases, which form the entire jet (or jet-body); thus each component has its corresponding ejection precession phase.

– (2) Inner sections of knots' trajectories along which the superluminal components move are assumed to follow a common helical pattern which precesses to produce the individual knot trajectories at their corresponding precession phases.

By applying the precessing nozzle scenario, the swing of the ejection position angle of the superluminal components could be investigated and the VLBI-kinematics of the superluminal components could be fitted by using model-simulation methods, including the observed features: their trajectory, core separation, coordinates and apparent velocity versus time.

Most importantly, the bulk Lorentz factor, viewing angle and Doppler factor of superluminal components as continuous functions of time could be derived. Thus the acceleration/deceleration in the motion of superluminal components and the relation between their flux variations and Doppler boosting effect could be investigated. This may be regarded as the distinct advantage of our scenario and method with respect to other scenarios. For example, in the recent work (Qian 2022), the flux evolution of the superluminal knot C9 in 3C345 was investigated and for the first time found that its 15GHz and 43 GHz light-curves were very well coincident with its Doppler boosting profile, suggesting the radio flux variations (flaring events) observed in knot C9 being fully due to its Doppler boosting effect. This strongly supports the traditional or common viewpoint: superluminal components are physical entities (shocks or plasmoids) moving with relativistic speeds toward us along helical trajectories at small viewing angles. At the same time this finding also strongly supports the electromagnetic mechanisms for the acceleration of superluminal components. It seems that the observed trajectories of superluminal components could not result from an underlying jet-pattern (induced by hydrodynamic/magneto-hydrodynamic instabilities) lit-up by plasmoids ejected from the nuclear activities.

The precessing nozzle scenario has been applied to investigate the VLBI-kinematic behavior of superluminal knots in several QSOs, e.g., 3C279, B1308+326, PG1302+202, NRAO150, 3C454.3 and OJ287 (Qian et al. 2014, 2017, 2018a, 2019a, Qian 2013, 2016, 2018b, Qian et al. 2021). Through model-simulation of the VLBI-kinematics of their superluminal components, we have shown that all these quasars could have precessing jet-nozzles with certain precession periods. For the four blazars (3C279, OJ287, 3C454.3 and 3C345) we have tentatively shown that they could have double precessing-jet structures and some precessing common trajectory patterns could exist, along which the superluminal components move according to their precession phases. However, we found that only within the inner sections of observed trajectories the superluminal components followed the precessing common trajectory pattern, while in the outer sections they followed their own individual trajectory patterns. Thus as for their whole trajectories concerned different trajectory patterns should be chosen to make model-fits to the entire kinematics of individual knots.

Interestingly, both jets (designated as jet-A and jet-B) were tentatively found to precess with the same precession period in the same direction. Thus the precession of both jet-nozzles might be due to the keplerian motion of the putative binary black holes in their nuclei (e.g., see Begelman et al. 1980).

Especially in the case of blazar OJ287, its quasi-periodic optical variability has been suggested to be connected with its double-jet activity (Villata et al.1998). Qian (2018b) has summarized both the theoretical and observational evidence for the possible existence of a double-jet structure in its nucleus, and interpreted the VLBI-kinematics of its superluminal components in detail in terms of precessing nozzle scenario within the framework of double-jet structure (Qian 2019b, 2019c, 2020; also Qian et al. 2007).

Search for periodicities in optical and radio light-curves (e.g. Sillanpää et al. 1988, Babadzhanyants et al.1995, Kudryavtseva et al.2006, Qian et al. 2007) are important and could provide key information on the nature of the central engine in blazars.

In the case of blazar 3C345, in our earlier studies we found that the observed tracks of knots C4 and C5 could be reproduced by the rotation of a common helical trajectory (Qian et al. 1991a, 1991b, Qian & Zhang 1999). Qian et al. (2009) analyzed the distribution of the position angles for seven superluminal components (C4 to C10) at different core separations of 0.15 mas, 0.20 mas and 0.25 mas, and found that their inner trajectories (within core separation $r_n \lesssim 0.4$ mas) could be explained in terms of the precession of a common trajectory and a precession period of its jet-nozzle of $\sim$7.36 yr was derived. Based on the position angle swing of its superluminal components, some authors argued for the existence of a jet precession period: e.g., $\sim$8–10 yr (Lobanov & Zensus 1999, Klare et al. 2005, Klare 2003, Lobanov & Roland 2005).

We would like to point out that our precessing jet-nozzle scenario is well consistent with the magneto-hydrodynamic theories for the formation/collimation/acceleration of relativistic jets in active galactic nuclei (e.g., Artymoviz 1998, Blandford & Payne 1982, Blandford & Znajek 1977, Camenzind 1986, 1987, 1990, Li et al. 1992, Lovelace et al. 1986,Meier & Nakamura 2006, Nakamura & Asada 2013, Shi et al. 2012, 2015, Valhakis & Königl 2003, 2004).

In this paper we investigate the relation between the Doppler boosting effect and the flux density evolution for five superluminal components (C4, C5, C9, C10 and C22 of jet-A) in blazar 3C345 within the framework of our precessing jet-nozzle scenario. We confirm for the first time that the radio flux density light-curves of these knots were closely coincident with their Doppler boosting profiles which had been anticipatively derived through the model-fitting of their VLBI-kinematics. [1] These results may strongly justify the validity of our precessing jet-nozzle scenario and the correctness or appropriateness of the chosen model-parameters and the modeled functions.

As in the previous work (Qian 2022) the observational data for knots C4, C5, C9, C10 and C22 we adopted from Schinzel (2011a) and some data were re-calculated to make the compact core as the unified origin of coordinates. Due to core-shift effects only 43GHz and 22GHz observations were used (except for knot C5, for which only 15GHz data are available). Generally, we would not mark the errors of measurements in the figures obtained from the model-fittings for clarity, but one should keep in mind that the errors in measurements of knot's position were in the range of

[1] Interpretation of the flux evolution in terms of Doppler-boosting effect for more superluminal components in blazar 3C345 will be presented elsewhere (Qian, in preparation).

$\sim$0.05–0.1 mas.
We apply the concordant cosmological model (Spergel et al.2003, Hogg 1999) with Ω_λ=0.73 and Ω_m=0.27, and H_0=71 km$s^{-1}Mpc^{-1}$. Thus the luminosity distance of 3C345 is 3.49Gpc, angular-diameter distance D_a=1.37 Gpc, 1 mas=6.65 pc, 1 mas/yr=34.6c.

2. Geometry of the model

The precessing jet-nozzle model has been previously described (Qian et al. 2019a,2009, 1991a) for investigating the VLBI-kinematics and trajectory-distribution of superluminal components on parsec scales in the QSO 3C345. The formalism of the geometry is recapitulated as follows (referring to Qian et al. 2021, Qian 2022).
A special geometry consisting of four coordinate systems is as shown in Figure 1. We assume that the superluminal components move along helical trajectories around the curved jet axis (i.e., the axis of the helix).
We use coordinate system (X_n, Y_n, Z_n) to define the plane of the sky (X_n, Z_n) and the direction of observer (Y_n), with X_n-axis pointing toward the negative right ascension and Z_n-axis toward the north pole.
The coordinate system (X, Y, Z) is used to locate the curved jet-axis in the plane (X, Z), where ϵ represents the angle between Z-axis and Y_n-axis and ψ the angle between X-axis and X_n-axis. Thus parameters ϵ and ψ are used to define the plane where the jet-axis locates relative to the coordinate system (X_n, Y_n, Z_n).
We use coordinate system (x', y', z') along the jet-axis to define the helical trajectory pattern for a knot, introducing parameters $A(s_0)$ (amplitude) and $\phi(s_0)$ (phase), where s_0 represents the arc-length along the axis of helix (or curved jet-axis). z'-axis is along the tangent of the axis of helix. y'-axis is parallel to the Y-axis and η is the angle between x'-axis and X-axis (see Figure 1).
In general we assume that the jet-axis can be defined by a function $x_0(z_0)$ in the (X, Z)-plane as follows.

$$x_0 = p(z_0){z_0}^{\zeta} \tag{1}$$

where

$$p(z_0) = p_1 + p_2[1 + \exp(\frac{z_t - z_0}{z_m})]^{-1} \tag{2}$$

ζ, p_1, p_2, z_t and z_m are constants. The exponential term is devised for describing the jet-axis gradually curving toward the north, as the trajectory of knot C4 shows on large-scales.

$$s_0 = \int_0^{z_0} \sqrt{1 + (\frac{dx_0}{dz_0})^2}\, dz_0 \tag{3}$$

Therefore, the helical trajectory of a knot can be described in the (X,Y,Z) system as follows.

$$X(s_0) = A(s_0)\cos\phi(s_0)\cos\eta(s_0) + x_0 \tag{4}$$

$$Y(s_0) = A(s_0)\sin\phi(s_0) \tag{5}$$

$$Z(s_0) = -A(s_0)\cos\phi(s_0)\sin\eta(s_0) + z_0 \tag{6}$$

where $\tan\eta(s_0)=\frac{dx_0}{dz_0}$. The projection of the helical trajectory on the sky-plane (or the apparent trajectory) is represented by

$$X_n = X_p\cos\psi - Z_p\sin\psi \tag{7}$$

$$Z_n = X_p\sin\psi + Z_p\cos\psi \tag{8}$$

where

$$X_p = X(s_0) \tag{9}$$

$$Z_p = Z(s_0)\sin\epsilon - Y(s_0)\cos\epsilon \tag{10}$$

(All coordinates and amplitude (A) are measured in units of mas). Introducing the functions

$$\Delta = \arctan[(\frac{dX}{dZ})^2 + (\frac{dY}{dZ})^2]^{-\frac{1}{2}} \tag{11}$$

$$\Delta_p = \arctan(\frac{dY}{dZ}) \tag{12}$$

$$\Delta_s = \arccos[(\frac{dX}{ds_0})^2 + (\frac{dY}{ds_0})^2 + (\frac{dZ}{ds_0})^2]^{-\frac{1}{2}} \tag{13}$$

we can then calculate the viewing angle θ, apparent transverse velocity β_a, Doppler factor δ and the elapsed time T, at which the knot reaches distance z_0 as follows:

$$\theta = \arccos[\cos\epsilon(\cos\Delta + \sin\epsilon\tan\Delta_p)] \tag{14}$$

$$\Gamma = (1 - \beta^2)^{-\frac{1}{2}} \tag{15}$$

$$\delta = [\Gamma(1 - \beta\cos\theta)]^{-1} \tag{16}$$

$$\beta_a = \beta\sin\theta/(1 - \beta\cos\theta) \tag{17}$$

$$T = \int_0^{s_0} \frac{(1+z)}{\Gamma\delta v\cos\Delta_s} ds_0 \tag{18}$$

The amplitude and phase of the helical trajectory for superluminal knots are defined as follows.

$$A(Z) = A_0[\sin(\pi Z/Z_1)]^{1/2} \tag{19}$$

$$\phi(Z) = \phi_0 - (Z/Z_2)^{1/2} \tag{20}$$

A_0 represents the amplitude coefficient of the common helical trajectory pattern and ϕ_0 is the precession phase of an individual knot.
The aim of our model fitting of the kinematics of the superluminal components observed in 3C345 was to show that most components have their inner trajectories following the precessing common trajectory and their kinematics can be interpreted in terms of our precessing jet nozzle scenario, indicating the possible presence of a supermassive black hole binary in its nucleus (for details see Qian 2022 where a double-jet structure (jet-A and jet-B) in 3C345 was proposed).
The main subject of this paper is to investigate the flux evolution of five superluminal knots (C4, C5, C9 C10 and C22) of jet-A and shows that their flux evolution could well be interpreted in terms of the Doppler boosting effect during their accelerated/decelerated motion along helical trajectories. Thus the kinematic and emission properties of the five components can be unitedly explained within the framework of our precessing nozzle scenario.
As shown above, the precessing common helical trajectory which the superluminal components follow is defined by parameters (ϵ, ψ) , and formulas (1)-(2) and (19)-(20) and the corresponding parameters in them. For jet-A we

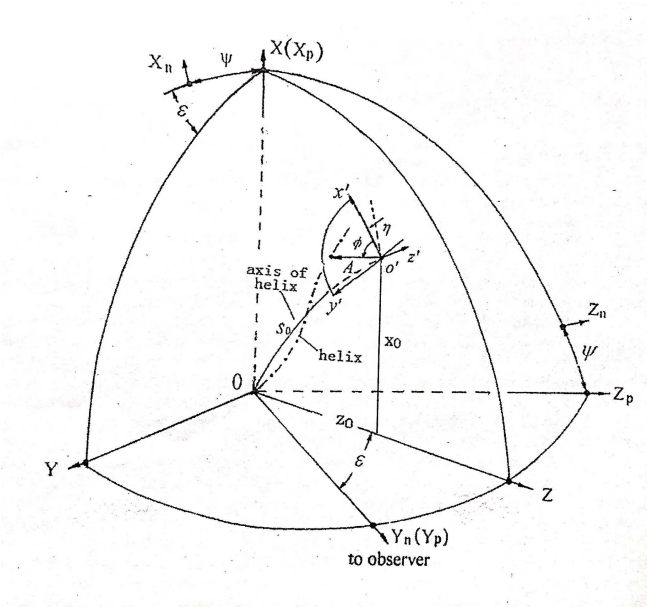


Fig. 1. Geometry of the precessing jet-nozzle scenario for 3C345. The jet-axis is defined in the (X, Z)-plane by parameters (ϵ, ψ) and function $x_0(z_0)$. The common helical trajectory pattern is defined by functions A(Z) and ϕ(Z) given in section 2 (Figure 2).

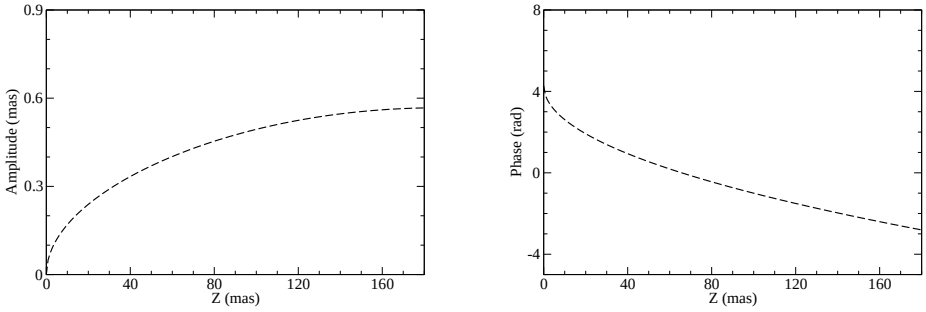


Fig. 2. Model parameters of the helical trajectory for knot C4: amplitude A(Z) and phase ϕ(Z).

assume the following values:
ϵ=0.0349 rad=2°; ψ=0.125 rad=7.16°; ζ=2.0, p_1=0; p_2=1.34×10^{-4}; z_t=66 mas; z_m=6 mas; A_0=0.605 mas, Z_1=396 mas and Z_2=3.58 mas. The precession phase ϕ_0 is related to the knot's ejection time:

$$\phi_0 = 4.28 + \frac{2\pi}{T_0}(T_0 - 1979.00) \qquad (21)$$

where T_0=7.30 yr–precession period of the jet-nozzle. The functions modeled for the amplitude and phase of the precessing helical trajectory pattern is shown in Figure 2 (for C4, ϕ_0=4.28 rad).
We would like to indicate here that all the five superluminal components move along the precessing common trajectory only in their inner trajectory sections. In the outer trajectory sections they move along their own individual trajectories. In order to model-fit their outer trajectories we shall introduce changes in parameters ϵ and ψ (which define the modeled jet-axis direction) only, without introducing any changes in the common helical trajectory pattern.

2.1. A note on the model-parameters

During the model-simulation of the kinematics of superluminal components in 3C345 the values chosen for the model parameters and the forms for the associated functions were not statistical samples and not unique. They were only specific and physically applicable sets of working ingredients which were obtained through trial and error methods over the past few years. But it was shown that they could be used to analyze the distribution of the observed trajectories and kinematics of superluminal components in blazar 3C345 on VLBI-scales, especially discovering the possible division of its superluminal knots into two groups with different kinematic properties. Our methods aimed at: (1) seeking for the possible jet-precession and determining the precession period; (2) searching for a double-jet structure; (3) disentangling the observed superluminal components into two groups attributed to respective jets; (4) investigating the relation between knots' flux evolution and Doppler boosting effect; (5) studying the properties of the putative supermassive binary black holes in its nucleus.
Similar methods have also been applied to blazar 3C279

(Qian et al. 2018a), OJ287 (Qian 2018b) and 3C454.3 (Qian et al. 2021). Interestingly, we tentatively found that all the four blazars seemed to have double-jet structures.

Since in our works model-simulations of the kinematics of superluminal components involved multi-parameters and multi-functions, we introduced a new criterion to judge the validity of the model-fitting results, instead of ordinarily used statistical errors estimated for the model parameters. That is, a reasonable and effective model-fitting of the kinematics of a superluminal knot was required to satisfy the condition that its observed inner-trajectory had to be fitted to follow the precessing common trajectory predicted by the scenario within ±5% of the precession period. A good example is presented in Figure 15 for knot C9 below. In addition, since the outer-trajectory of the superluminal components deviated from the precessing common trajectory pattern the model-fits to their outer-trajectories were performed through changing the parameters (ϵ, ψ) which defined the modeled jet-axis direction, while the common helical pattern was kept unchanged.

As shown in the previous paper (Qian 2022) the kinematics of the superluminal components of both jets in 3C345 could be well model-fitted and a precession period of 7.30±0.36 yr for both the jet-nozzles were derived.

In Figure 3 are shown the distribution of the precessing common trajectory for jet-A of 3C345 at different precession phases (left panel) and the observed trajectories of the superluminal knots C4, C5 and C13 (right panel) for comparison.

3. Basic equations for Doppler boosting effect and flux evolution

In order to investigate the relation between the flux evolution of superluminal components and their Doppler boosting effect during their accelerated/decelerated motion along helical trajectories, the observed flux density $S_{obs}(\nu,t)$ of superluminal components can be defined as the Doppler-boosted flux density:

$$S_{obs}(\nu,t) = S_{int}(\nu)\times\delta(t)^{3+\alpha} \tag{22}$$

$S_{int}(\nu)$=$S_0\,(\nu/\nu_0)^{-\alpha}$–the intrinsic flux density, S_0–the flux density at the fiducial frequency ν_0, and α–spectral index for the whole range of the observing frequencies (10–43 GHz), $\delta(t)$–Doppler factor. [2]

We also use the normalized flux density $S_{obs,N}(\nu,t)$ which is defined as

$$S_{obs,N}(\nu,t) = S_{obs}(\nu,t)/S_{obs,max}(\nu) \tag{23}$$

$S_{obs,max}(\nu)$–the observed maximum flux density.

The Doppler-boosting profile (a normalized profile) is defined as:

$$S_D(t) = [\delta(t)/\delta_{max}]^{3+\alpha} \tag{24}$$

Here δ_{max} – the modeled maximum Doppler factor.

We also use the intrinsic flux density, approximately defined as: $S_{int}(\nu)$=$S_{obs,max}(\nu)/[\delta_{max}]^{3+\alpha}$.

[2] In most general case both S_{int} and α could be defined as functions of ν and t , and thus Doppler-boosting profiles varying with time and frequency, and complex flux evolution could be investigated. But here in this paper we assume that $S_0(t)$ and $\alpha(\nu,t)$ are constants, not depending on time and frequency.

In the precessing nozzle scenario the Doppler factor $\delta(t)$ of superluminal knots depends on their motion along helical trajectories which are produced by the precessing common trajectory at corresponding precession phases (or ejection epochs).

As already shown in the previous paper, the kinematics of the superluminal components was well model-simulated, and their bulk Lorentz factor $\Gamma(t)$ and Doppler factor $\delta(t)$ as functions of time were predictively derived, which could be used to investigate the relation between the Doppler boosting effect and their flux evolution. We found that in order to correctly model-fit their flux evolution, the bulk Lorentz factor and Doppler factor previously derived should be appropriately modified. Moreover, in order to investigate the flux evolution at multi-frequency on the whole trajectory (in both inner and outer trajectory sections), variations in parameters ϵ and ψ, intrinsic flux density S_{int} and spectral index α should also be taken into consideration.

4. Interpretation of kinematics and flux evolution for knot C4

As shown in previous paper (Qian 2022), the entire kinematics of knot C4 with its observed core separation extended to ∼8 mas could be well model-simulated in terms of our precessing nozzle model. However, only its inner trajectory within a core-separation of ∼1.8 mas followed the precessing common trajectory pattern. Thus in order to model-fit its entire kinematics and investigate its flux evolution we had to appropriately modify the previously derived bulk Lorentz factor and model-parameters ϵ and ψ.

4.1. Model simulation of kinematics for knot C4

In the present model the inner trajectory of knot C4 within X_n≤1.14 mas (r_n≤1.15 mas, traveled distance Z_c≤40.0 mas∼266 pc) could be well fitted by the precessing common trajectory pattern (Fig.5). Its precession phase was modeled as ϕ_0=4.28 rad and ejection epoch t_0=1979.0. In Figure 4 are presented the traveled distance Z(t) along the Z-axis, and the curves of model parameters $\epsilon(Z)$ and $\psi(Z)$ (right panel), which indicate that within Z≤40.0 mas (t≤1987.08) ϵ=2.0° and ψ=7.16°, and knot C4 moved along the precessing common trajectory, while beyond Z=40.0 mas ϵ started to increase and ψ stated to decrease, and knot C4 started to move along its own individual trajectory (in its outer trajectory-section). The model-fit to its inner trajectory section is shown in Figure 5: the curves in black, magenta and blue represents the precessing common trajectories for precession phases ϕ_0=4.28 rad and ϕ_0±0.31 rad, respectively. The curve in violet represents the model-fit to the whole trajectory.

Correspondingly, its bulk Lorentz factor was adjusted as follows in order to take its deceleration after 1982.67 into consideration: for Z≤0.5 mas Γ=6.0; for Z=0.5-2.0 mas Γ increased from 6 to 8; for Z=2-18 mas Γ increased from 8 to 13 ; for Z=18-35 mas Γ decreased from 13 to 10; for Z=35-40 mas Γ decreased from 10 to 5.5; for Z>40 mas Γ=5.5. Γ_{max}=13.0 at 1982.67, and the corresponding maximum Doppler factor δ_{max}=23.5.

It can be seen from Figure 6 that the entire kinematics of knot C4 could be well explained in terms of our precess-

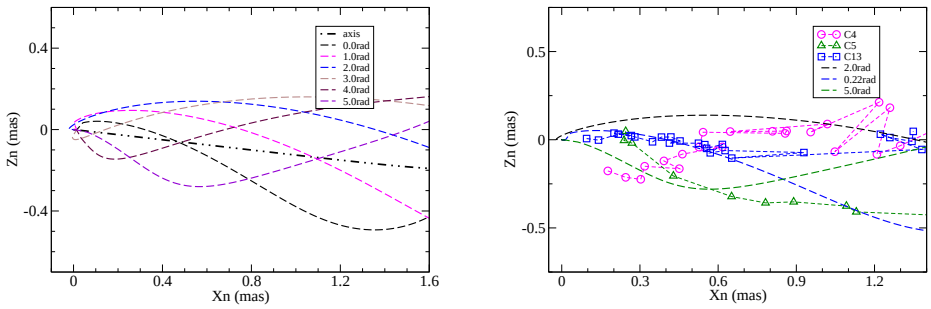


Fig. 3. Distribution of the precessing common trajectory for jet-A in 3C345 (left panel). The jet axis is at position angle $\sim -97.2°$ with its cone aperture $\sim 42.5°$ (at core separation 0.5 mas). The opening angle of the jet is $\sim 1.12°$ in space. The observed trajectories of knots C4, C5 and C13 are presented in the right panel for a comparison with the model distribution.

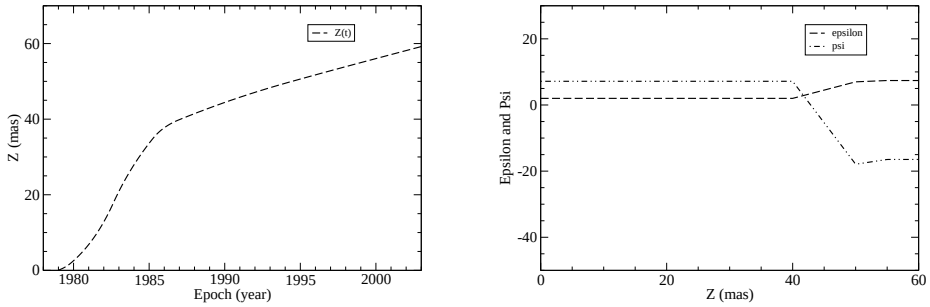


Fig. 4. Knot C4. The traveled distance Z(t) along the Z-axis (left panel) and the model parameters ϵ and ψ as functions of time. Within Z=40.0 mas (t$\leq$1987.08) ϵ=2.0° and ψ=7.16°, and knot C4 moved along the precessing common trajectory, while beyond Z=40.0 mas ϵ increased and ψ decreased and knot C4 moved along its own individual track.

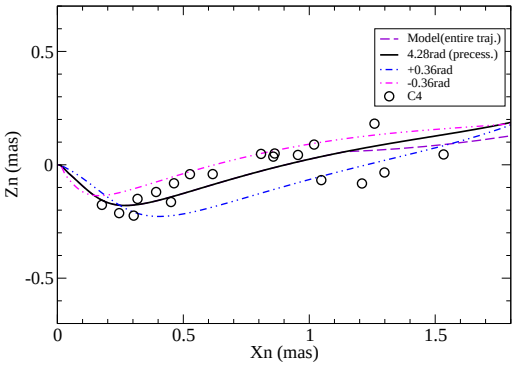


Fig. 5. Knot C4: Model-fit to its inner trajectory within $X_n \simeq 1.14$ mas. The black line describes the precessing common trajectory-section with the precession phase ϕ_0=4.28 rad and the corresponding ejection time t_0=1979.0. The lines in magenta and blue show the precessing common trajectories for precession phases ϕ_0+0.31 rad and ϕ_0-0.31 rad (i.e., $\pm$5% of the precession period), respectively. The curve in violet represents the model-fit to the whole trajectory.

ing nozzle scenario, including the whole trajectory $Z_n(X_n)$, core separation $r_n(t)$ and coordinate $X_n(t)$ (upper three panels), and coordinate $Z_n(t)$, the derived apparent velocity $\beta_{app}(t)$/viewing angle $\theta(t)$ and the derived bulk Lorentz factor $\Gamma(t)$/Doppler factor $\delta(t)$ (bottom three panels).

The apparent speed derived showed two bumps (Figure 6, bottom/middle panel): one occurred before 1987.08 in its inner-trajectory section where knot C4 followed the precessing common trajectory with its maximum speed of $\sim$8c at $\sim$1982.7, while the other occurred during the period of 1995–2005 in its outer trajectory section where knot C4 moved along its own individual trajectory. The

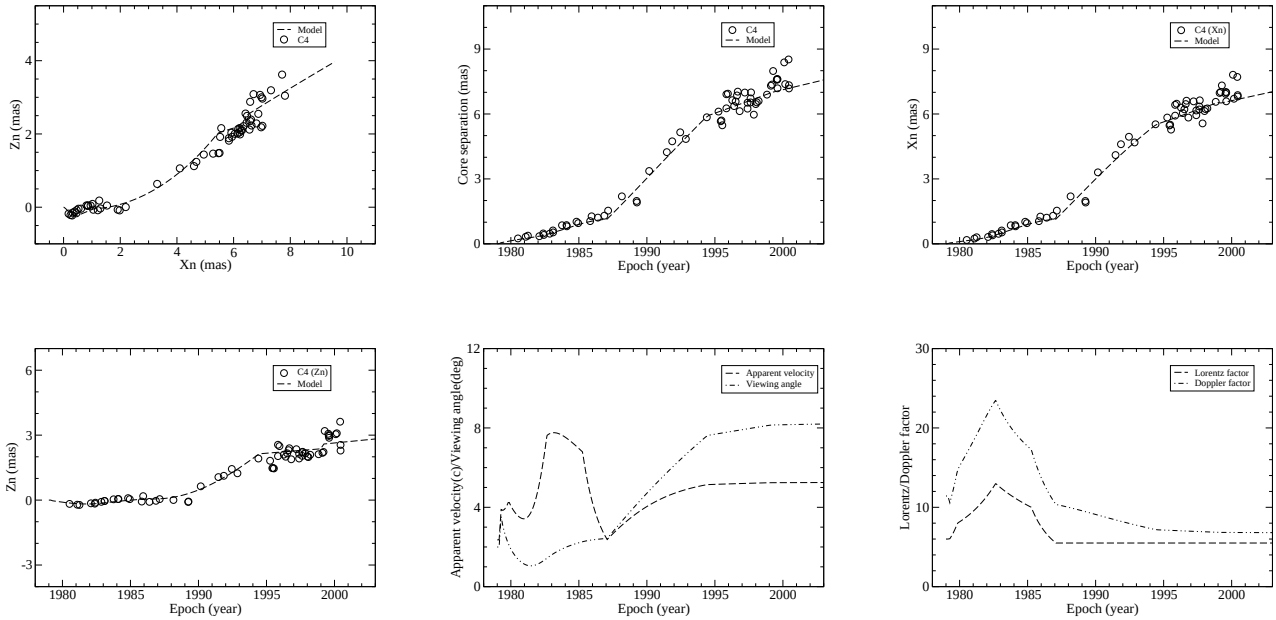


Fig. 6. Knot C4: Model fits to the entire kinematics of knot C4 (within $r_n \simeq 8$ mas), including its whole trajectory, core separation and coordinate X_n (upperthree panels), and coordinate Z_n, the model-derived apparent speed and viewing angle, and the model-derived bulk Lorentz factor and Doppler factor (bottom three panels).

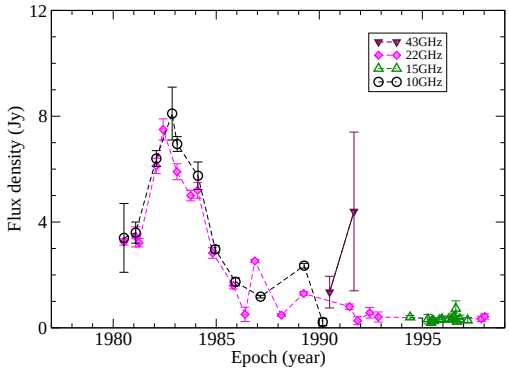


Fig. 7. Knot C4: Light curves observed at 10 GHz and 22 GHz with a few data-points observed at 15 and 43 GHz.

derived viewing angle showed variations along a concave curve in the inner trajectory section, while it showed a bump structure in its outer trajectory section. This is the first time to obtain a continuous curve for the apparent-velocity/viewing-angle of knot C4 during a time-interval of ∼20 years.

Both the derived bulk Lorentz factor and Doppler factor showed only one-bump structure occurred in its inner trajectory section before 1987.08, i.e., it occurred when its motion followed the precessing common trajectory (Figure 6, bottom/right panel), showing its intrinsic acceleration/deceleration along the precessing common helical trajectory.

4.2. Doppler boosting effect and flux evolution of knot C4

The derived Doppler-factor curve shown in Figure 6 (bottom/right panel) reveals a distinct bump structure with its peak at ∼1982.6. This is a very good case for yielding the Doppler boosting profile (normalized at its peak, $[\delta(t)/\delta_{max}]^{3+\alpha}$) and studying the relation between its flux-density evolution and the Doppler boosting effect.

The observed 10 GHz and 22 GHz light-curves of knot C4 are shown in Figure 7. Both the light-curves showed a peak flux density at ∼1983, closely corresponding to the peak in the Doppler factor curve (δ_{max}=23.5 at ∼1982.64). A spectral index α(22-10GHz)=0.18 was assumed. The intrinsic flux densities were assumed as: 3.54×10^{-4}Jy (10 GHz) and 3.28×10^{-4}Jy (22 GHz).

The model-fits to the 10 GHz and 22 GHz light-curves in terms of Doppler-boosting effect are shown in Figure 8, re-

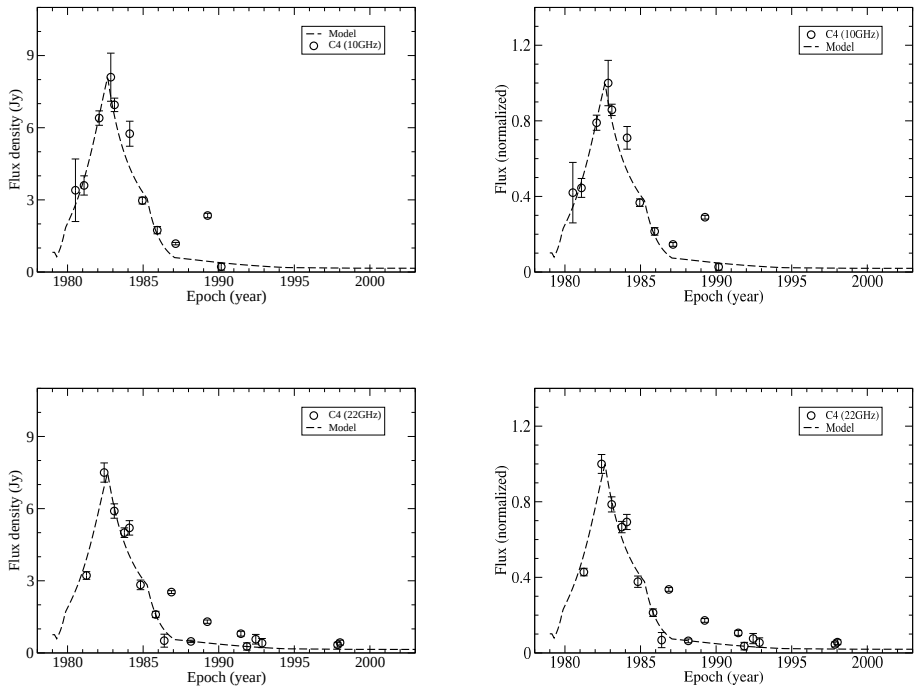


Fig. 8. Knot C4: coincidence of the 10 GHz and 22 GHz light-curves with the Doppler boosting profiles: the observed light-curves (left two panels) and the normalized light-curves (right two panels).

spectively. It can be seen that the 10GHz and 22GHz light-curves were extremely well coincident with the Doppler boosting profiles (for both the observed flux light-curves and the normalized flux light-curves). This implies that the flux-density variations observed at 10 GHz and 22 GHz were fully induced by its Doppler boosting effect, and the variations in its intrinsic flux density were not detectable, i.e., the emission of the relativistic shock producing the superluminal component C4 was very stable.

The domination of Doppler boosting effect in the emission of knot C4 strongly justifies the traditional point-view which is supported by most blazar physicists and VLBI-observers: superluminal components participate relativistic motion toward us along helical trajectories with acceleration/deceleration. This result strongly proves that our precessing nozzle scenario can interpret the entire VLBI-kinematics of knot C4 and correctly derive its Doppler factor as a continuous function of time which can be used to interpret its flux density evolution. The explanation of the entire kinematics and emission properties for knot C4 in terms of our precessing nozzle scenario is very encouraging and instructive.

5. Interpretation of kinematics and flux evolution for knot C5

5.1. Model simulation of kinematics for knot C5

For the interpretation of the kinematics of superluminal components in jet-A of 3C345 in terms of the precessing nozzle scenario the kinematic behavior of knot C5 is quite significant, because its ejection epoch t_0=1980.80 and corresponding precession phase ϕ_0=5.83 rad were different from those of knot C9 (t_0=1995.06 and ϕ_0=5.54+4π) by about two precession periods (Comparing Figure 10 with Figure 15 in the next section for knot C9). Moreover, its apparent trajectory was very similar to that of knot C9, demonstrating the recurrence of the precessing common trajectory and confirming the basic assumption in our scenario: the superluminal components move along the common trajectory which precesses to give rise to the individual trajectories of the superluminal knots at corresponding precession phases.

In Figure 9 are shown the traveled distance of knot C5 along the Z-axis (left panel) and the curves of parameters ϵ and ψ, which indicate: during the period 1980.80-1990.42 (Z$\leq$44.8 mas, $X_n\leq$1.21 mas, $r_n\leq$1.25 mas) knot C5 moved along the precessing common trajectory. After 1990.42 ϵ started to increase and ψ started to decrease, and knot C5 started to move along its own individual trajectory (in its outer trajectory section).

The model-fit to its inner trajectory section is shown in Figure 10: the curves in black, magenta and blue represent the precessing common trajectories for precession phases ϕ_0=5.83 rad and 5.83$\pm$0.31 rad ($\pm$5% of the precession period), respectively. The curve in violet represents the fit to the whole trajectory.

The model fits to its whole kinematic behavior are shown in Figure 11. It can be seen that its entire trajectory, core separation, two coordinates are well model-simulated. The derived apparent speed showed a distinct bump during the period $\sim$1983–1990, while the viewing angle varied along a depressed curve. The derived curves of bulk Lorentz factor and Doppler factor had distinct bumps during 1986.2–1988.3. Thus the intrinsic acceleration/deceleration and Doppler boosting effect occurred in its inner trajectory

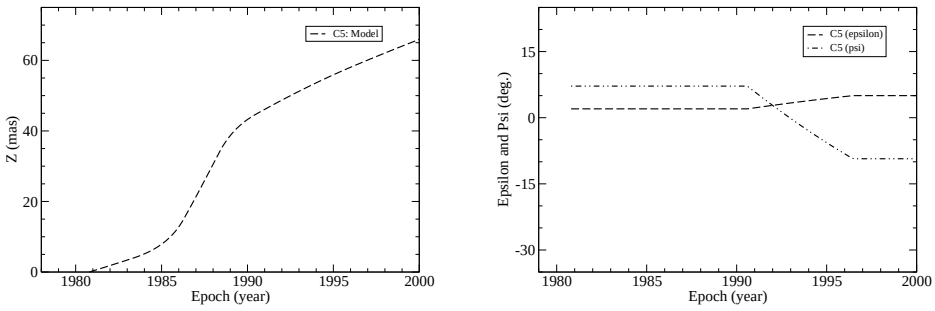


Fig. 9. Knot C5. The traveled distance Z(t) along the Z-axis (left panel), and the curves of ϵ(t) and ψ(t) (right panel). Within Z=44.8 mas (t=1990.4) ϵ=2° and ψ=7.16°, and knot C5 moved along the precessing common trajectory. Beyond Z=44.8 mas it moved along its own individual trajectory.

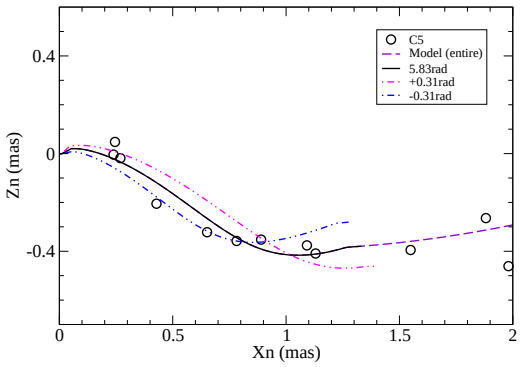


Fig. 10. Knot C5: Model-fit to its inner trajectory section (within r_n=1.25 mas (or X_n=1.21 mas, t=1990.4). The curve in black represents the precessing common trajectory for precession phase ϕ_0=5.83 rad (corresponding ejection time t_0=1980.80). The curves in magenta and blue represent the precessing common trajectories for precession phases ϕ_0+0.31 rad and ϕ_0-0.31 rad, respectively.

section where knot C5 moved along the precessing common trajectory.

Bulk acceleration and deceleration were required and the Lorentz factor was modeled as: for Z≤4.0 mas Γ=5.5; for Z=4.0-15 mas Γ increased from 5.5 to 13.2 (Γ_{max}=13.2 at 1986.21); for Z=15–34 mas, Γ=const.=13.2; for Z=34-45 mas Γ decreased from 13.2 to 7.0 (1990.53); for Z>45 mas Γ=7.0.

It can be seen that the entire kinematic behavior within core separation r_n ≲1.25 mas can be well fitted, implying that its observed precessing common trajectory could extend to a spatial distance of Z_c=44.8 mas (or ∼298 pc) from the core.

5.2. Doppler boosting effect and flux evolution of knot C5

The bump structure derived for the Doppler factor of knot C5 provided an very good explanation of the flux evolution of knot C5 during its motion along the precessing common trajectory. The observed 10 GHz and 22 GHz light-curves are shown in Figure 12, clearly revealing a flare event during ∼1985–1991 with a peaking flux at ∼1988.0, which was closely coincident with the Doppler-boosting profile. We assumed the spectral index α(10–22GHz)=0.30, the intrinsic flux densities were assumed to be 1.5×10^{-4}Jy (10 GHz) and 7.7×10^{-5}Jy (22 GHz). The model-derived maximum Doppler factor δ_{max}=24.6 at ∼1987.4.

The model-fits to the observed 10 GHz and 22 GHz light-curves are shown in Figure 13 (left two panels), while their normalized light-curves were fitted by the normalized Doppler-boosting profiles ($[\delta(t)/\delta_{max}]^{3+\alpha}$) in the right two panels. It can be seen that the 15 GHz and 22 GHz light-curves were very well coincident with the Doppler boosting profiles which were calculated by using the model-predicted Lorentz factor curve $\Gamma(t)$ and the model-predicted viewing angle curve $\theta(t)$ (Fig.11, bottom/right and bottom/middle panels, respectively).

The shorter time-scale variations at 22 GHz during ∼1983–1984 could be due to the intrinsic flux variations of knot C5 (see the discussion on the flux variations of knots C9 and C10 below).

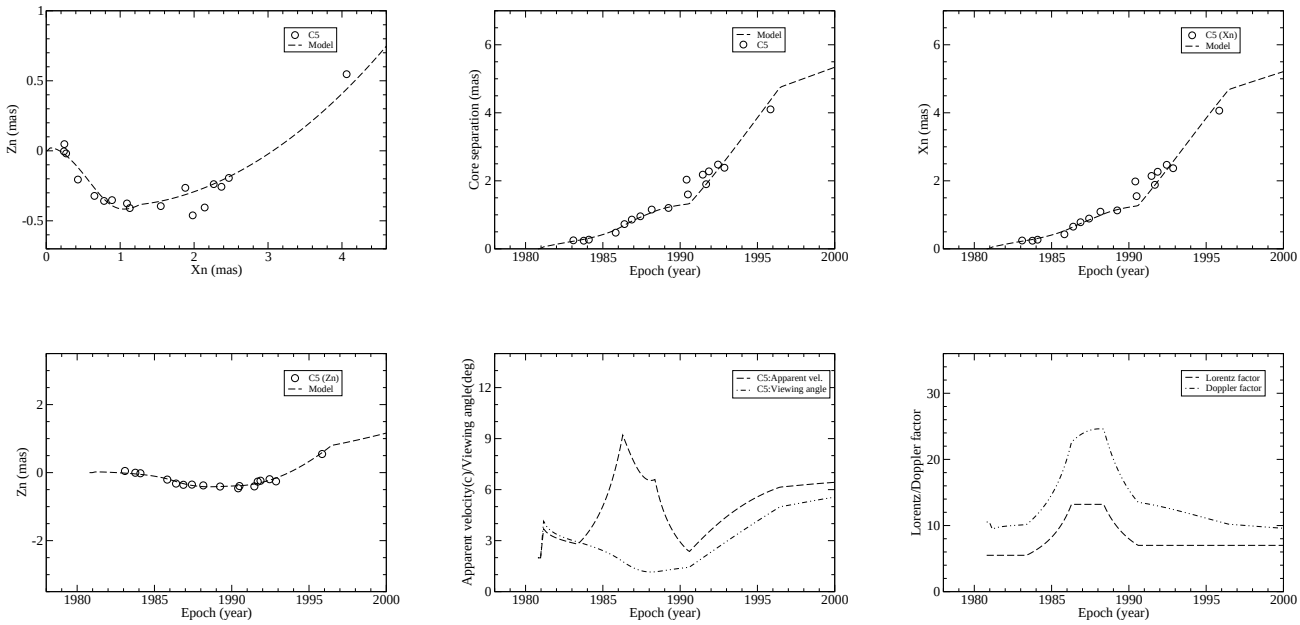


Fig. 11. Knot C5. Model-fitting results: trajectory $Z_n(X_n)$, core separation r_n and coordinate X_n(t) (upper three panels), and coordinate Z_n(t), the modeled apparent velocity β_a(t) and viewing angle θ(t), bulk Lorentz factor Γ(t) and Doppler factor δ(t) (bottom three panels). Precession phase ϕ_0=5.83 rad and ejection time t_0=1980.80.

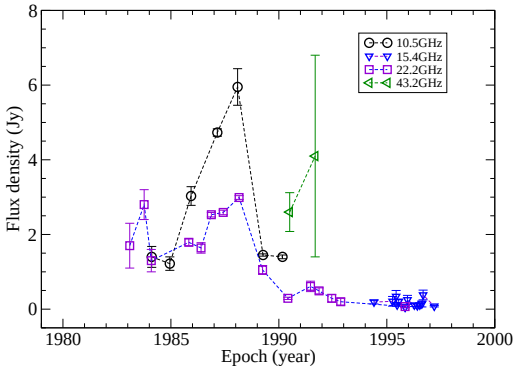


Fig. 12. Knot C5: the light-curves observed at 10 GHz and 22 GHz with some data-points observed at 15 GHz and 43 GHz.

6. Interpretation of kinematics and flux evolution for knot C9

As shown in the previous paper (Qian 2022), The results of model-fitting of its kinematics and the explanation of its flux evolution in terms of Doppler boosting effect are very important and encouraging for the application of our precessing nozzle scenario to study the phenomena in 3C345 and other blazars. Knot C9 was a typical and exceptionally instructive example of applying the scenario for a satisfying interpretation of its VLBI-kinematics and flux evolution. Here we recapitulate the main results obtained in Qian (2022) and supplement some new results on its flux evolution and spectral features.

6.1. Model simulation of kinematics for knot C9

In the left panel of Figure 14 the traveled distance Z(t) along the Z-axis from the core of knot C9 is shown. In the right panel is shown the parameters ϵ and ψ as functions of time. It can be seen that $\epsilon(t)$ is a constant (0.0349 rad=2°), but $\psi(t)$ varied with time: before 1999.94 ψ=0.125 rad=7.16° and its trajectory followed the precessing common trajectory for the precession phase ϕ_0=5.54+4π (corresponding to its ejection time t_0=1995.06). After 1999.94 ψ increased and its trajectory deviated from the precessing common trajectory and knot C9 moved along its own individual trajectory (in its outer trajectory section).
The model-fit to its inner trajectory section (or precessing common trajectory) is shown in Figure 15, where the

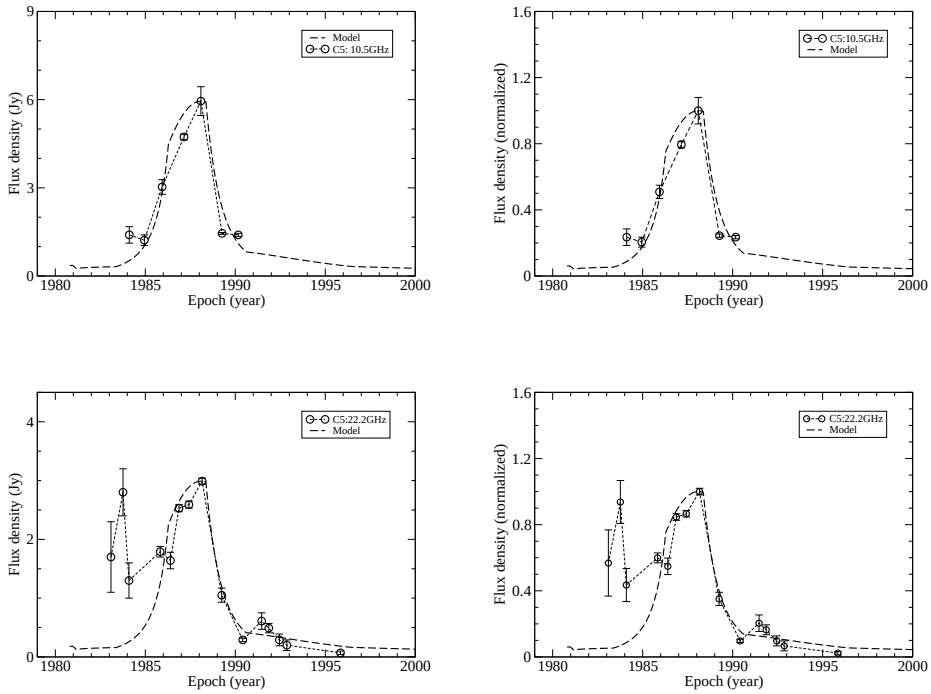


Fig. 13. Knot C5. The 10 GHz and 22 GHz light-curves were well coincident with the Doppler boosting profiles for both the observed flux light-curve (left two panels) and the normalized flux light-curve (right two panels).

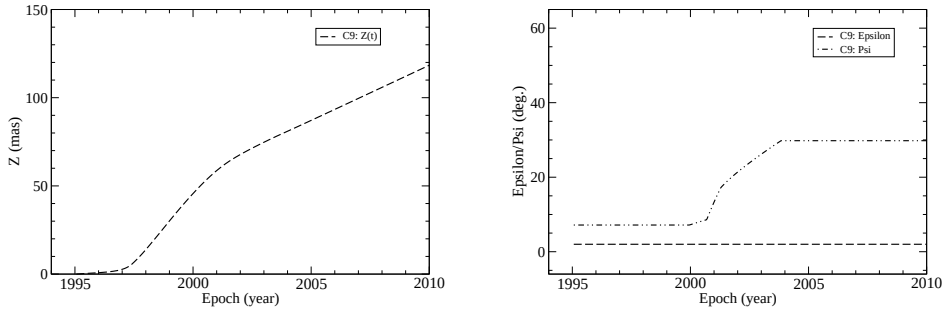


Fig. 14. Knot C9. Left panel: the traveled distance Z(t) along the Z-axis. The right panel shows ϵ=const.=2° and ψ=7.16° before 1999.94 ($r_n \leq 1.25$ mas or $X_n \leq 1.22$ mas), when it moved along the precessing common trajectory (in its inner-trajectory section). After 1999.94 ψ increased and knot C9 started to move along its own individual trajectory (in its outer trajectory section).

curve in black represents the precessing common trajectory section for the precession phase $\phi_0 = 5.54+4\pi$. The curves in magenta and blue represent the model-trajectories for precession phases $\phi_0 \pm 0.31$rad, showing its ejection epoch being fitted with an accuracy of ± 0.36 yr (5% of the precession period). The curve in violet represents the model-fit to its entire trajectory. Its precessing common trajectory section extended to $r_n \sim 1.25$ mas or the traveled distance $Z_c \sim 44.8$ mas=298 pc.

In Figure 16 the model-fitting results of its entire kinematics are presented: the entire trajectory $Z_n(X_n)$, core separation $r_n(t)$, coordinate $X_n(t)$ (upper three panels), and coordinate $Z_n(t)$, the modeled apparent velocity $\beta_{app}(t)$, viewing angle $\theta(t)$, bulk Lorentz factor $\Gamma(t)$ and Doppler factor $\delta(t)$ (bottom three panels).

It can be seen that the kinematic properties of knot C9 during the entire observing period ∼1997–2008 (within core separation $r_n \sim 4.1$ mas) were very well model-fitted.

Its apparent speed, viewing angle, bulk Lorentz factor and Doppler factor as functions of time were derived through the model-fitting of its entire kinematics. The accelerated motion observed in knot C9 during 1986–1988 could be well explained by the increase in its Lorentz factor and its motion along the helical trajectory.

In order to explain its apparent motion and flux evolution its bulk acceleration and deceleration were required and its bulk Lorentz factor was modeled as (bottom/right panel in Figure 16): For Z≤1.0 mas Γ=4; for Z=1–6 mas Γ increased from 4 to 18.5 (Γ_{max}=18.5 at 1997.44); for Z=6–14 mas Γ=18.5; For Z=14–20 mas Γ decreased from

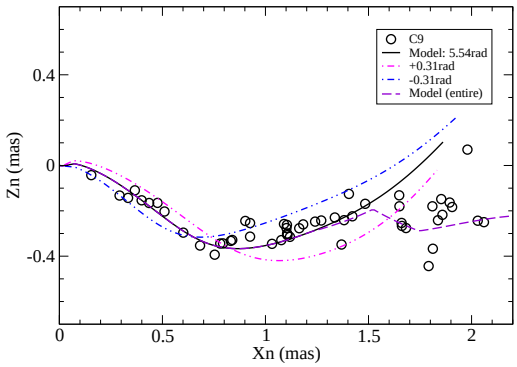


Fig. 15. Knot C9. Model fit to the inner trajectory section ($Z_c \leq$ 44.8 mas, $X_n \leq$1.21 mas, t$\leq$1999.94) where it moved along the precessing common trajectory. The black curve represents the precessing common trajectory for precession phase ϕ_0=5.54+4π (ejection time t_0=1995.06), while curves in magenta and blue represent those for precession phases $\phi_0 \pm 0.31$ rad ($\pm$5% of the precession period). The curve in violet represents the model-fit to its whole trajectory.

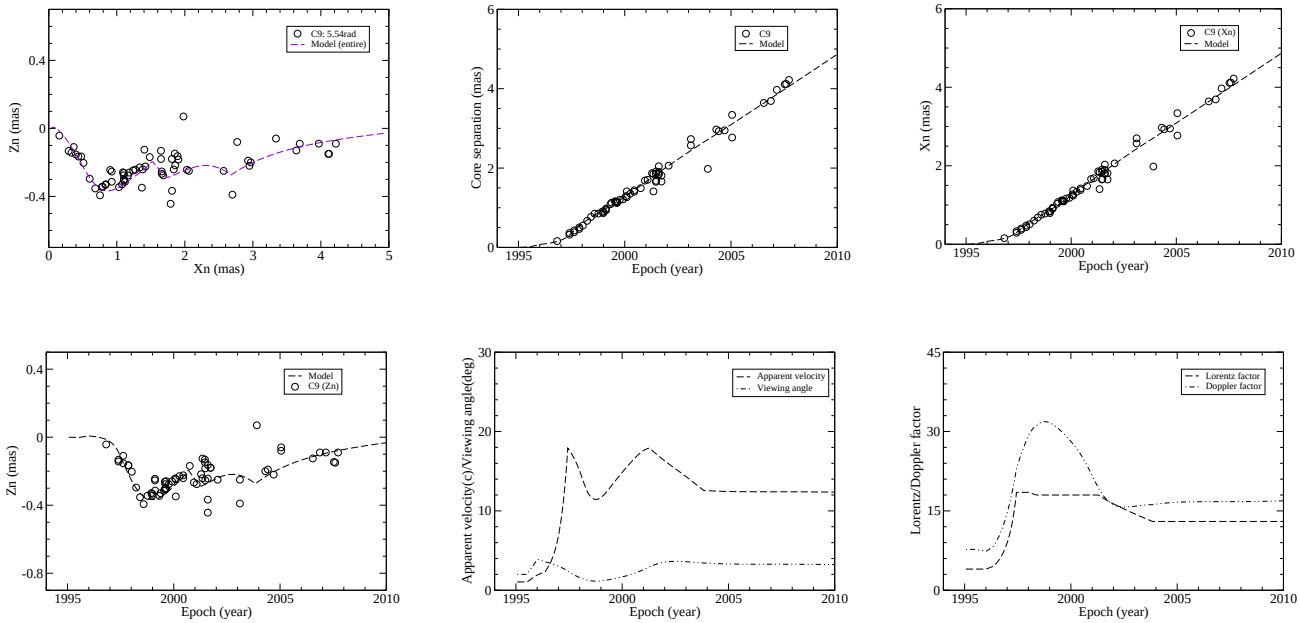


Fig. 16. Knot C9. Model-fitting results for the whole trajectory $Z_n(X_n)$, core separation $r_n(t)$ and coordinate X_n(t) (upper three panels); model-fitting results for coordinate Z_n(t), model-derived apparent-velocity $\beta_{app}(t)$ and viewing-angle $\theta(t)$, and model-derived bulk Lorentz-factor $\Gamma(t)$ and Doppler-factor $\delta(t)$ (bottom three panels). $\Gamma(t)$ has a platform of maximum ($\simeq$18.5–18.0) during 1997.4-2001.3.

18.5 to 18.0; For Z=20-61.7 mas (t=2001.28) Γ=18.0; For Z=61.7–80 mas (t=2003.84) Γ decreased from 18.0 to 13.0; for Z>80 mas Γ=13.0.
The modeled Doppler-factor curve showed a smooth bump structure during 1996–2002, providing a very determinative Doppler-boosting effect to explain its flux variations observed at 43 GHz, 22 GHz and 15 GHz.
The derived apparent velocity $\beta_a(t)$ showed two peaks while the viewing angle $\theta(t)$ varied along a depressed curve (bottom/middle panel in Figure 16).

6.2. Doppler-boosting effect and flux evolution of knot C9

The modeled Doppler factor δ(t) as a continuous function of time shown in Figure 16 (bottom/right panel) had a smooth bump structure during 1997–2002, thus providing a distinctly smooth Doppler-boosting profile to study the Doppler-boosting effect in the flux variations of knot C9. This was a rare and extremely valuable opportunity to test our precessing nozzle scenario and investigate the relation between its flux evolution and Doppler-boosting effect.
The light-curves observed at 43 GHz, 22 GHz and 15 GHz of knot C9 are shown in Figure 17. In Figure 18 are presented the reformed 15GHz and 43GHz light-curves:

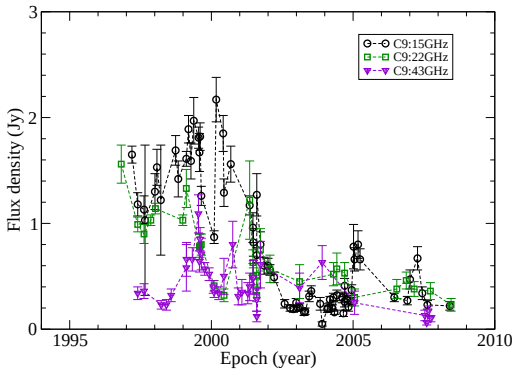


Fig. 17. Knot C9. Lght-curves observed at 15 GHz, 22 GHz and 43GHz.

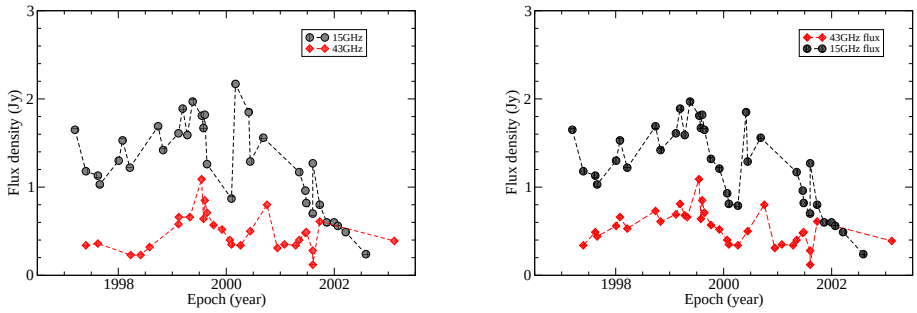


Fig. 18. Knot C9. Light-curves observed at 15 GHz and 43 GHz (left panel) and the reformed light curves with an assumed spectral index α(15-22-43GHz)=0.80.

the rising phase of the observed 43GHz light-curve was reformed by adding the 43GHz flux calculated from the 15 GHz rising-phase data-points with a spectral index α(15-43GHz)=0.80. Similarly, the decaying phase of the observed 15GHz light-curve was reformed by adding the 15GHz flux calculated from the 43 GHz decaying-phase data-points.

It can be seen that the observed and reformed light-curves reveal a flaring behavior during ∼1997.50-2000.25, having a close correlation by visual inspection.

Based on the datasets observed at 43 GHz, 22 GHz and 15 GHz we obtained α(22-43 GHz)$\simeq$0.70$\pm$0.59 and α(15-43 GHz)$\simeq$0.81$\pm$0.25. In the model-fits to the flux evolution the spectral index was assumed α(15-22-43 GHz)=0.80.

The modeled maximum Doppler factor δ_{max}=31.86 occurred at t_{max}=1998.78. The intrinsic flux densities were assumed to be: 3.82×10^{-6}Jy (15 GHz), 2.58×10^{-6}Jy (22 GHz) and 1.65×10^{-6}Jy (43 GHz), corresponding the observed maximum flux densities: 1.97 Jy (1999.38), 1.33 Jy (1999.12) and 0.85 Jy (1999.60), respectively.

In Figure 19 are presented the model-fits to the light-curves observed at 43 GHz, 22 GHz and 15 GHz (left three panels) and their normalized light-curves (right three panels).

In Figure 20 are presented the model-fits to the reformed light-curves observed at 43 GHz and 15 GHz (left two panels) and their normalized light-curves (right two panels). Obviously, the reformed light-curves were fitted more appropriately by the Doppler-boosting profiles.

It can be seen from Figures 19 and 20 that both the observed and reformed light-curves during 1997.5–2000.3 were very well coincident with the Doppler-boosting profiles which was anticipatively-determined through the model-simulation of the kinematics of knot C9.

However, there were some shorter time-scale flux variations during 2000.5–2008.5 remained to be explained. Since these variations were not related to the Doppler-boosting effect induced by the accelerated/decelerated motion of knot C9, they could be due to: (i) the variations in intrinsic flux density S_{int} of knot C9 and (ii) the variations in its spectral index α (see equation (22) in section 3). For example, assuming that the shorter time-scale variations at 15 GHz were due to the variations in its intrinsic flux density with the spectral index unchanged (α(15 GHz)=0.80), then the variations at 22 GHz and 43 GHz could be due to the variations in spectral index (α(22 GHz) and α(43 GHz)) at the two frequencies which should be different from that at 15 GHz.

Obviously, the interaction of the traveling relativistic shocks (superluminal components) with the surrounding evironments could produce these intrinsic variations.

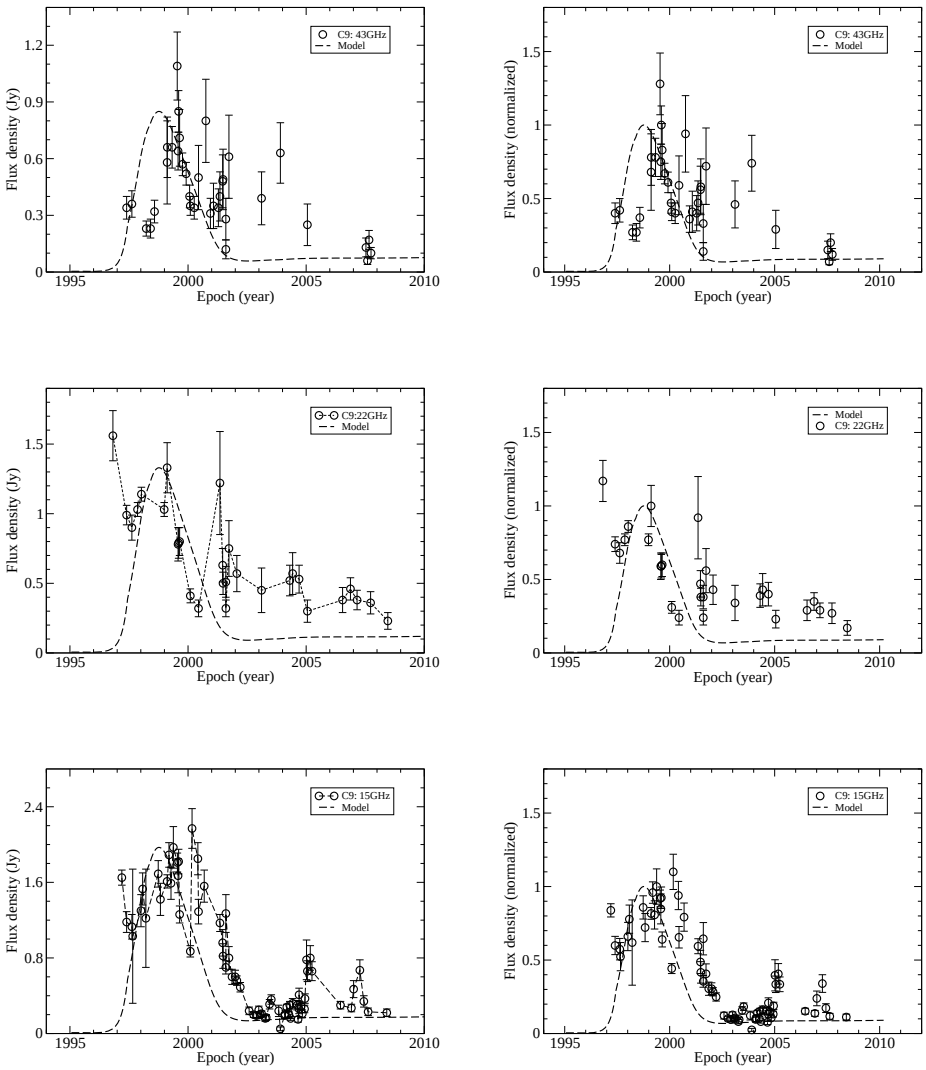


Fig. 19. Knot C9. Top two panels: the observed 43GHz light-curve and its normalized light-curve fitted by the Doppler-boosting profiles. Middle two panels: the observed 22 GHz light-curve and its normalized light-curve fitted by the Doppler-boosting profiles. Bottom two panels: the observed 15 GHz light-curve and its normalized light-curve matched by the Doppler-boosting profiles.

7. Interpretation of kinematics and flux evolution for knot C10

The flux evolution of knot C10 is a very instructive one, providing another valuable opportunity to test our precessing nozzle scenario. Its flux variations consisted of two main flaring events caused by the Doppler boosting effect, involving its complex behavior of bulk acceleration/deceleration and change in its trajectory pattern: one occurred in the inner precessing common trajectory section, while the other in the outer individual trajectory section.

We first discuss the model-simulation of its kinematics and then its Doppler-boosting effect and flux evolution.

Its precession phase was modeled as ϕ_0(rad)=6.14+4π, corresponding to the ejection time t_0=1995.76. Its precessing common trajectory apparently extended to $X_n\sim$0.35 mas (or the traveled distance Z_c ∼6.13 mas along the Z-axis, or ∼40.8 pc from the core).

7.1. Model simulation of kinematics for knot C10

In Figure 21 are presented the curves for the following functions: (1) Z(t) describes its traveled distance along the Z-axis from the core as a function of time (left panel); (2) functions $\epsilon(t)$ and $\psi(t)$ (right panel) describe the jet-axis direction of inner and outer trajectory sections, showing only in the inner trajectory section (during the time-interval of 1995.76-1999.14 (corresponding to $X_n\leq$0.35 mas) where knot C10 moved along the precessing common trajectory.

Figure 22 shows the transition from the precessing common trajectory-section to the outer trajectory-section at X_n ∼0.35 mas. The curves in black, magenta and blue describe the precessing common trajectories for precession phases ϕ_0=6.14+4π and $\phi_0\pm$0.31 rad, respectively. The

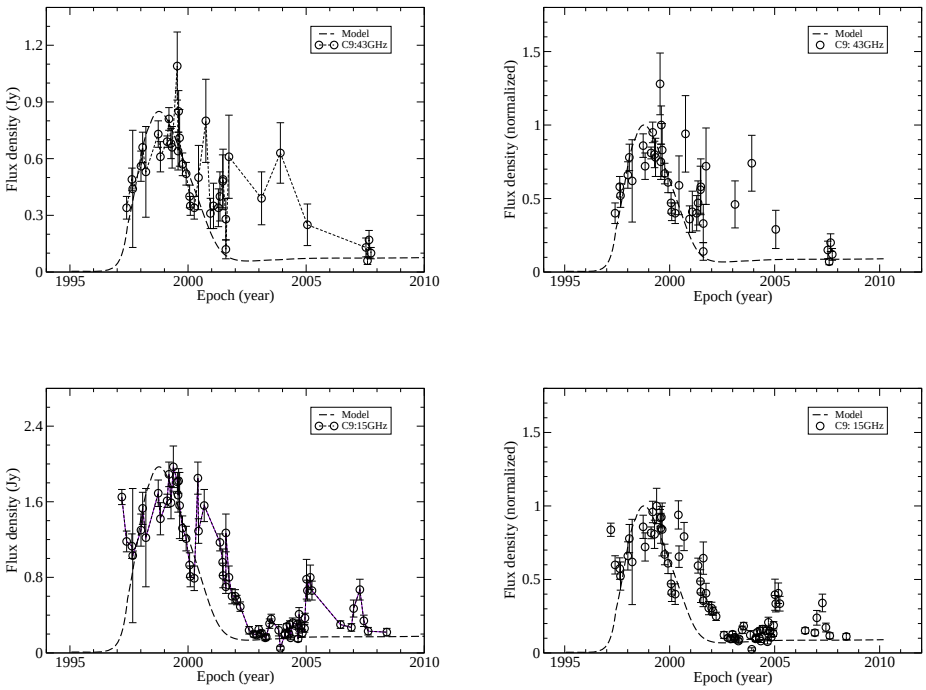


Fig. 20. Knot C9. Upper panels: the reformed 43GHz light-curve and its normalized light-curve well matched with the Doppler boosting profiles. Bottom panels: the reformed 15 GHz light-curve and its normalized version well coincident with its Doppler boosting profiles. These reformed curves more appropriately matched the Doppler-boosting profiles.

curve in violet describes the model-fit to the whole trajectory.

The results of model-fitting of the whole kinematics for knot C10 are presented in Figure 23, including the model-fits of entire trajectory $Z_n(X_n)$, core separation $r_n(t)$, coordinates $X_n(t)$ and $Z_n(t)$, and the derived apparent velocity $\beta_{app}(t)$ and viewing angle $\theta(t)$, the derived bulk Lorentz factor $\Gamma(t)$ and Doppler factor $\delta(t)$. It can be seen by visual inspection that the trajectory, core separation, coordinates are well fitted by our precessing nozzle model.

As a distinct feature we noticed that, at ∼1999.14 its core separation r_n suddenly increased (Fig.23, top/middle panel), which was possibly due to the change in the modeled jet-axis direction (see Fig.21, right panel), where its motion along the precessing common trajectory ended and transited to its own individual trajectory (Fig.22).

7.2. Doppler-boosting effect and flux evolution of knot C10

In order to consider the Doppler-boosting effect in the flux-evolution of knot 10 we needed to know its spectral index in radio bands. Based on the data observed at three frequencies (15, 22 and 43 GHz) we obtained: spectral index α(22-43GHz)$\simeq$0.64$\pm$0.4 and α(15-43GHz)$\simeq$0.90$\pm$0.27. Thus in the following model-fitting of the Doppler-boosting effect we adopted a spectral index α=0.80 in the whole band of 15 to 43 GHz. The Doppler-boosting profile was then defined by $[\delta(t)/\delta_{max}]^{3.80}$ (Figs.25 and 26), where δ_{max}=14.11 was the maximum Doppler factor of the first flare event at 1998.36 in our fitting model.

The radio light-curves observed at 15, 22 and 43 GHz are shown in Figure 24. The observed light-curves at 15, 22 and 43 GHz were normalized by using the observed maximum fluxes of the first flare, taken as 2.17, 1.60 and 0.94 Jy, respectively. Thus the corresponding intrinsic fluxes at 15, 22 and 43 GHz were chosen as S_{in}=9.3×10^{-5}Jy, 6.8×10^{-5}Jy and 4.0×10^{-5}Jy, respectively.

As shown in Figure 23 the anticipatively derived bulk Lorentz factor showed two-bumps: one occurred in the inner trajectory-section (or the precessing common trajectory before 1999.14) with its Γ_{max}=8.5 at epoch 1998.36), while the other occurred in the outer trajectory section with its Γ_{max}=17.0 at epoch 2000.92. Specifically, its bulk Lorentz factor was modeled to indicate its behavior of acceleration/deceleration to re-acceleration/deceleration : for Z$\leq$0.6 mas (1995.76-1997.00) Γ=3.0; for Z=0.6-4.2 mas (1997.00-1998.38) Γ increased from 3.0 to 8.5; for Z=4-6.4 mas (1998.38-1999.41) Γ decreased from 8.5 to 4.0; for Z=6.4-12.1 mas (1999.41-2000.92) Γ increased from 4.0 to 17.0; for Z=12.1-23.2 mas (2000.92-2003.87) Γ decreased from 17.0 to 7.0 and then kept to be const.=7.0 (Fig.23, bottom/right panel).

Correspondingly, the derived apparent velocity β_{app}(t) also showed a double-bump structure as shown in Figure 23 (bottom/middle panel).

However, the derived Doppler factor showed three bumps, the first one occurred in the precessing common trajectory section (δ_{max}=14.11 at epoch 1998.36), while the other two occurred in the outer trajectory section with their δ_{max}=11.35 at 1999.98 and δ_{max}=13.89 at 2002.00, respectively.

It can be seen from Figures 25 and 26 that the observed flux light-curves were similar to the Doppler-boosting profiles, but had much complex structures. Most interestingly, the

22 GHz light-curves (both observed and normalized) were extremely well fitted by the Doppler-boosting profiles as shown in Figure 25.
The 15 GHz and 43 GHz light-curves shown in Figure 26 were also fitted quite well by the Doppler-boosting profiles. However, at the two frequencies a number of data-points largely deviated from the modeled Doppler-boosting profiles. This phenomenon is quite similar to that observed in knot C9 (Figs.19 and 20).
As an example, during ∼2000.0-2001.5 the data-points observed at 15 and 43 GHz distributed much higher than the modeled Doppler-boosting profiles (Fig. 26). This could be due to the following effects: (1) at 15 GHz knot C10 had its spectral index to be larger than 0.80 or its intrinsic flux density being larger than the adopted value 9.3×10^{-5}Jy; (2) at 43 GHz knot C10 had its spectral index to be smaller than 0.80 or its intrinsic flux being larger than the adopted value 4.0×10^{-5}Jy. Additionally, both the spectral indexes and intrinsic fluxes at 15 and 43 GHz were variable with time.[3]
It worths noting that for knot C10 the selection of the model-parameters was quite difficult, because the model-fits involved multiple functions simultaneously (requiring model-fits to its trajectory, coordinates, core separation, apparent velocity and flux evolution (complex light-curves) at multi-frequencies. All these observed properties were functions of time. Thus the successful interpretation of its kinematics and flux evolution seems very encouraging for validating our precessing nozzle scenario.

8. Interpretation of kinematics and flux evolution for knot C22

As shown in the previous paper (Qian 2022), the model-fit to the kinematic behavior of knot C22 was quite important, because: (1) the ejection time of knot C22 (2009.36) was approximately equal to that (1995.06) of knot C9 plus ∼two precession periods (14.6 yr) and that (1980.80) of knot C5 plus ∼4 precession periods. Thus our precessing nozzle scenario could explain its kinematic behavior during a time-interval of four precession periods (∼29.2 years); (2) the observed trajectories of knot C5, C9 and C22 quite clearly indicated the recurrence of the precessing common trajectory pattern, validating this helical pattern adopted in our precessing nozzle scenario; (3) the three knots all revealed the intrinsic acceleration/deceleration in their motion; (4) their Doppler factors derived from the model-simulation of their kinematics showed bump-structures, implying the existence of Doppler-boosting effect.
Here in this paper we shall confirm that the flux variations observed in knot C22 could be successfully interpreted in terms of its Doppler-boosting effect as for the flux evolution observed in knots C4, C5, C9 and C10.
All these distinct features listed above may actually justify our precessing nozzle scenario for investigating the VLBI-phenomena in QSO 3C345.

8.1. Model simulation of kinematics for knot C22

As shown in the previous paper (Qian 2022) the model-fitting of the kinematics for knot C22 of jet-A in 3C345 was very important because the VLBI-observations of knot C22 extended the periodic behavior of jet-A to 4 precession periods relative to the ejection of knot C4 (from ∼1979 to 2009, about 30 years).
According to the precessing nozzle scenario the kinematics of C22 could be model-fitted by using precession phase ϕ_0(rad)=5.28+8π and ejection epoch t_0=2009.36.
In Figure 27 are shown its traveled distance Z(t) along the Z-axis (left panel) and the curves of functions $\epsilon(t)$ and $\psi(t)$. During the period 2009.36–2009.98 in its inner trajectory-section (Z≤2.3 mas, X_n≤0.156 mas, spatial distance Z_c≤15.3 pc), ϵ=2.0° and ψ=7.16°, and knot C22 moved along the precessing common trajectory. After 2009.98 ϵ and ψ started to increase and knot C22 started to move along its own individual trajectory, which deviated from the precessing common trajectory in its outer trajectory-section.
The model-fit to its inner trajectory-section in terms of the precessing common trajectory is shown in Figure 28.
The model-fitting results for its entire kinematics are shown in Figure 29. It can be seen that the entire trajectory, core separation, two coordinates were very well fitted in terms of our precessing nozzle scenario.
The model-derived apparent velocity/viewing angle and the bulk Lorentz factor/Doppler factor are shown in the bottom/middle and bottom/right panels of Figure 29, respectively.
Specifically, its bulk Lorentz factor was modeled as: for Z≤0.20 mas (2009.51) Γ=5.0; for Z=0.2–1.2 mas(2009.51-2009.80) Γ increased form 5.0 to 15.0; for Z=1.2–2.3 mas (2009.80-2009.98) Γ decreased from 15.0 t0 10.2; For Z=2.3–3.6 mas (2009.98-2010.41) Γ decreased from 10.2 to 8.0 and then kept constant beyond Z=3.6 mas (after 2010.41).
As shown in Figure 29 (bottom/right panel) that the model-predicted Doppler factor showed a bump-structure during the period ∼2009.5-2010.2 with its peak δ_{max}=16.90 at 2009.87, which should induce Doppler-boosting effect in the flux evolution of knot C22 and it really occurred as described below.

8.2. Doppler-boosting effect and flux evolution of knot C22

The close relation between the flux variations and the Doppler-boosting effect found in knot C22 provided one more valuable and successful test of our precessing nozzle scenario.
It can be seen that both the observed 43 GHz light-curve and its normalized light-curve were extraordinarily well fitted by the Doppler-boosting profile, as shown in Figure 30: a flaring event during 2009.6–2010.2 with its peak of ∼1.49Jy at ∼2009.91 was well coincident with the Doppler boosting profile $[\delta(t)/\delta_{max}]^{3.5}$. [4] That is, The flux-density evolution of knot C22 can be fully interpreted in terms of its Doppler boosting effect. Thus our precessing nozzle scenario gets through one more valuable test.

[3] No such behavior was clearly observed at 22 GHz: knot C10 has a spectral index 0.80 and a steady intrinsic flux 6.8×10^{-5}Jy at this frequency.

[4] Here we arbitrarily assumed a spectral index 0.50. The intrinsic flux density was then derived to be 5.72×10^{-5}Jy.

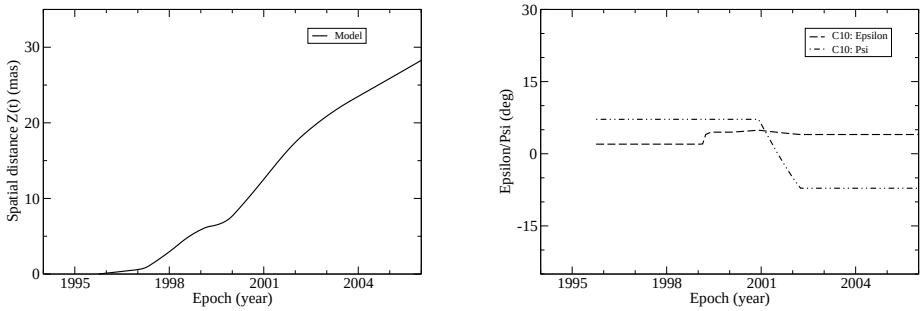


Fig. 21. Knot C10. Left panel: the traveled distance Z(t) from the core (or spatial distance) along the Z-axis. Right panel: parameters $\epsilon(t)$ and $\psi(t)$ which define the modeled direction of jet-axis. Before 1999.14 (X_n<0.35 mas) ϵ=2.0° and ψ=7.16°, and knot C10 moved along the precessing common trajectory. After 1999.14 (X_n>0.35 mas) ϵ started to increase and knot C10 started to move along its own individual trajectory in its outer trajectory-section. Parameter ψ started to decrease from 2000.92 (X_n>1.19 mas) and its outer trajectory pattern changed once again.

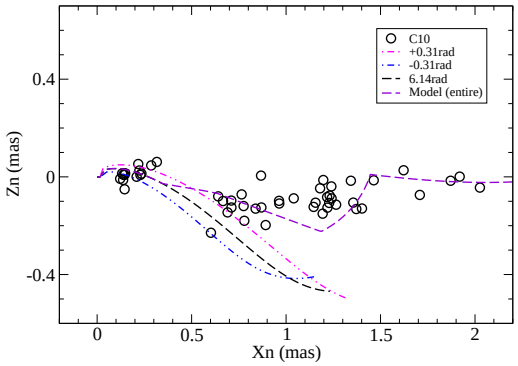


Fig. 22. Knot C10. Model-fit to the inner trajectory section in terms of the precessing common trajectory which apparently extended to X_n∼0.35 mas (corresponding spatial distance Z_c ∼6.13 mas or 40.8 pc). The curve in violet represents the model-fit to its whole trajectory, while the curves in black, magenta and blue represent its precessing common trajectories for precession phases ϕ_0(rad)=6.14+4π and 6.14±0.31+4π, respectively.

9. Conclusive remarks

We can make some conclusions as follows.
(1) We have applied our precessing jet-nozzle scenario previously proposed to interpret the VLBI-kinematics and flux evolution for five superluminal components (C4, C5, C9, C10 and C22) in QSO 3C345. It is shown that the VLBI-measured kinematic properties of all these superluminal knots (including trajectory, core separation, coordinates, apparent velocity as functions of time) can be well model-simulated and explained, adopting a precession period of 7.30±0.36 yr and a precessing common trajectory pattern. The model-simulation methods dealing with the model-fitting of multiple functions with multiple parameters were now validated.
(2) The apparent trajectories observed for the five superluminal knots could be divided into two sections: inner section and outer section. In the inner sections the superluminal components moved along the precessing common trajectory (or common helical-pattern trajectory), while in the outer sections they moved along their own individual trajectories which deviated from the common precessing trajectory pattern.
(3) Through the model-simulation of their kinematic properties their bulk Lorentz factor and Doppler factor as functions of time were naturally derived and thus the relation between their Doppler boosting effect and flux evolution could be investigated. It is shown that the knots' radio light-curves (radio flaring events) occurred during their motion in the inner regions could be successfully explained in terms of their Doppler-boosting effect. The simultaneous determination of the multiple parameters as functions of time describing the kinematic and dynamic properties may be regarded as the advantage of our precessing jet-nozzle scenario and model-simulation methods.
(4) Using the anticipatively-determined Doppler factors, for the first time we were able to study the flux evolution of superluminal components in QSO 3C345. We found that the radio light-curves of the five components were fully coincident with the Doppler boosting profiles [5]. Most impor-

[5] Shorter time-scale flux variations could be understood as due to the fluctuations in the intrinsic emission and spectral index of the knots, which could be produced by the interaction of the traveling relativistic shocks with the complex physical environments.

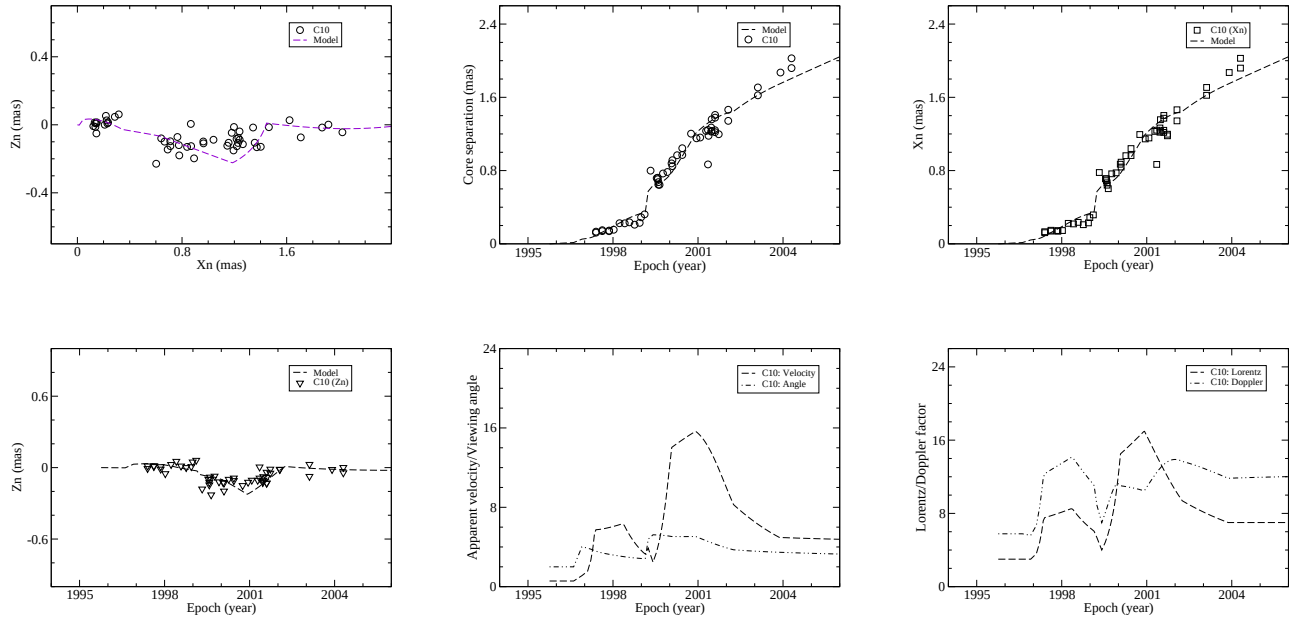


Fig. 23. Knot C10: Model simulation of the VLBI-kinematics. Upper panels: apparent trajectory $Z_n(X_n)$, core separation $r_n(t)$ and coordinate $X_n(t)$. Bottom panels: coordinate $Z_n(t)$, apparent speed $\beta_{app}(t)$/viewing angle $\theta(t)$ and bulk Lorentz factor $\Gamma(t)$/Doppler factor $\delta(t)$. It is noted that the sudden increase in core separation r_n at 1999.14 was due to a sudden change in the modeled jet-axis direction and its trajectory started to deviate from the precessing common trajectory. Both apparent velocity and bulk Lorentz factor show a two-bump structure, while the modeled Doppler factor shows a three-bump structure with peaks at 1998.36, 1999.98 and 2002.00, respectively.

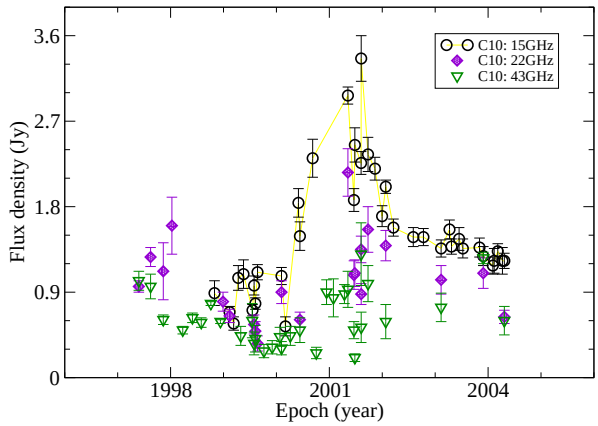


Fig. 24. Knot C10: light-curves observed at 15 GHz, 22 GHz and 43 GHz.

tantly, for all the five superluminal components (C4, C5, C9, C10 and C22) the radio flaring events produced by the Doppler-boosting effect occurred during their motion in the inner trajectory regions (i.e., the precessing common trajectory sections).

Obviously, these results summarized above are significant for our precessing jet-nozzle scenario and we can now make an overall review of our scenario to provide a full-view for studying the VLBI-phenomena in QSO 3C345 as follows.

– The plasmoids and magnetized plasmas ejected by the precessing nozzle was assumed to form the entire jet of 3C345, thus VLBI-observations could find many superluminal components moving along different trajectories, forming a complex distribution of superluminal components in the jet.
– In fact these observed trajectories were formed at different precession phases by the precession of a common helical trajectory pattern associated with the nozzle-precession, although for different superluminal components they had outer trajectory-sections where they moved along their own individual trajectory patterns.

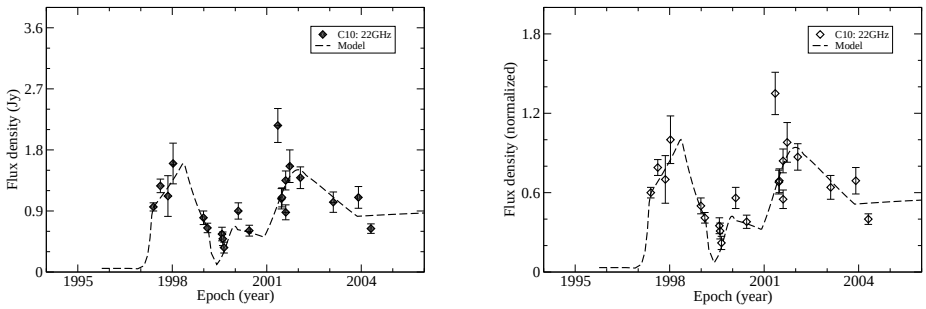


Fig. 25. Knot C10: The 22 GHz variations were extremely well fitted by the Doppler boosting profile with an adopted spectral index α=0.80 for the observed flux light-curve (left panel) and the normalized flux light-curve (right panel).

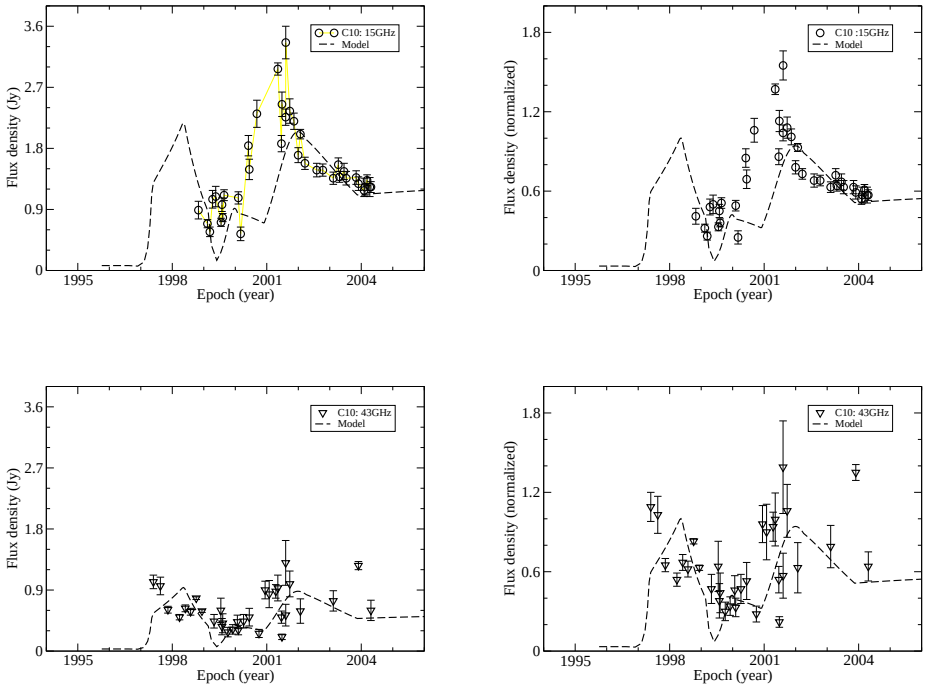


Fig. 26. Knot C10: The 15GHz and 43GHz light-curves well fitted by the Doppler-boosting profiles. Variations in its intrinsic flux density and spectral index at the two frequencies probably gave rise to the shorter time-scale flux fluctuations.

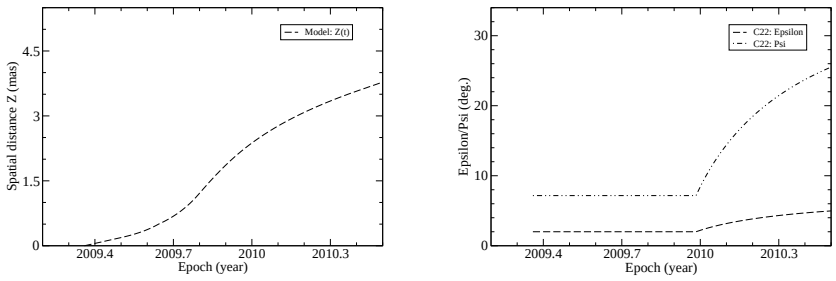


Fig. 27. Knot C22: the traveled distance along the Z-axis (left panel) and the curves of ϵ and ψ (right panel), describing the change in the modeled jet-axis direction. Before 2009.98 (Z$\leq$2.3 mas) ϵ=2.0° and ψ=7.16°, knot C22 moved along the precessing common trajectory in its inner trajectory-section. After 2009.98, ϵ and ψ started to increase and knot C22 started to move along its own individual trajectory in its outer trajectory-section.

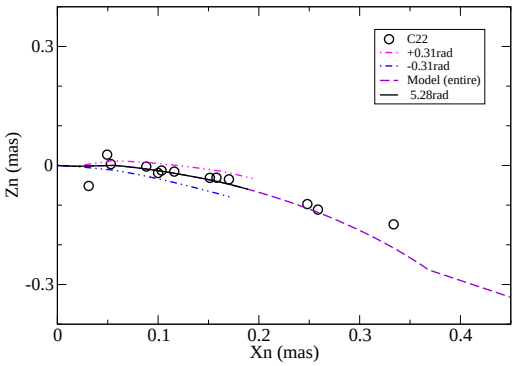


Fig. 28. Knot C22: Model-fit to its inner trajectory-section by the precessing common trajectory. Black curve represents the precessing common trajectory-section for the precession phase 5.28 rad+8π, the curves in magenta and blue represent the precessing common trajectory sections for precession phases 5.28+8$\pi\pm$0.31 rad, respectively. the curve in violet represents the model fit to the whole trajectory.

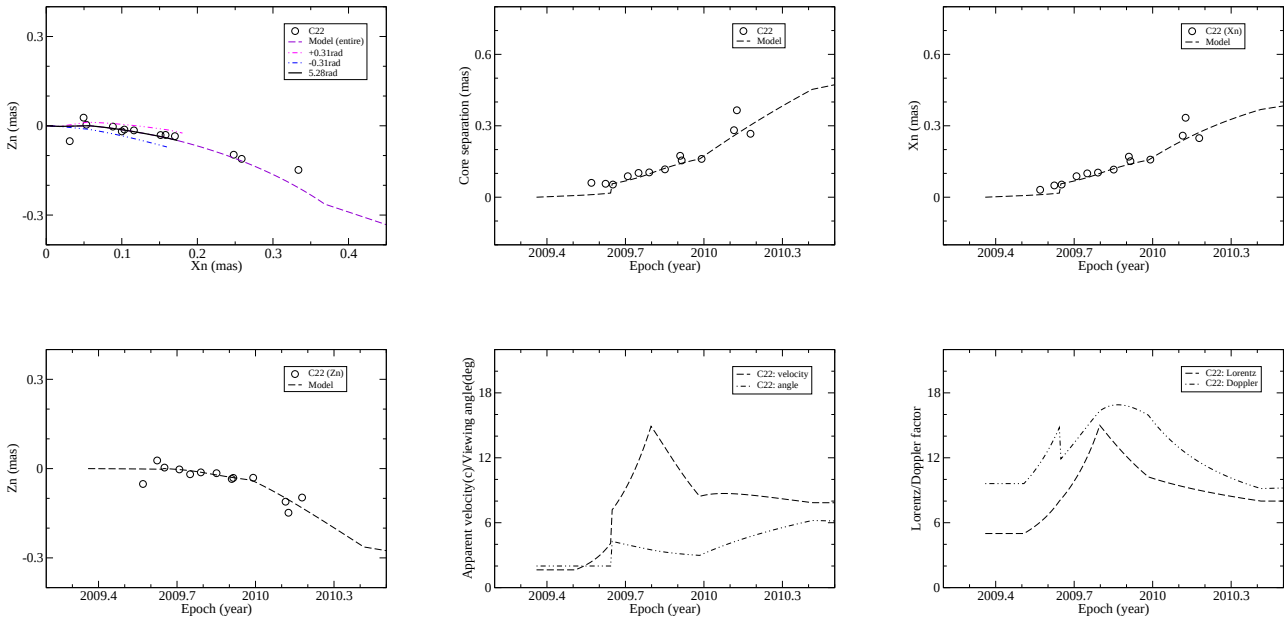


Fig. 29. Knot C22: Model fits to its kinematic properties with its precession phase ϕ_0=5.28 rad+8π, t_0=2009.36, including the fits to the whole trajectory, core separation and coordinate X_n (upper three panels); coordinate Z_n, the derived apparent-velocity/viewing-angle and bulk Lorentz-factor/Doppler-factor (bottom three panels).

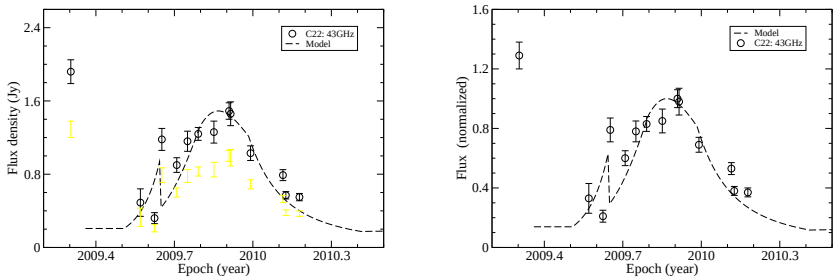


Fig. 30. Knot 22: The observed 43 GHz flux light-curve (left panel) and the normalized flux light-curve (right panel) were very well fitted by the Doppler-boosting profiles.

- The observed swing of the ejection position angle of superluminal components and its quasi-periodicity could be understood in terms of the nozzle-precession.
- The observed kinematics (including apparent trajectory, core distance, coordinates, apparent speed) can be well fitted consistently for all the superluminal components, if a double precessing-nozzle structure (or double-jet structure) was assumed. [6]
- The double-jet structure as an assumption was based on the model-simulation results: jet-A and jet-B have different kinematic and dynamic properties, including different jet direction, precessing common trajectory pattern and opening angle of precession cone, but having a similar precession period and direction of precession. This type of precession could originate from keplerian motion in the putative binary black hole in the nucleus of 3C345.
- The precession period 7.3 ± 0.36 yr for both the jet-A and jet-B seems model-simulated appropriately, since for both jets the kinematic behaviors have been well explained and model-fitted.
- Since the inner trajectory-sections observed for all the superluminal components of both jet-A and jet-B in 3C345 are well model-fitted within an accuracy of $\pm5\%$ of the precession period, the precessing common trajectory patterns derived for both jet-A and jet-B should be regarded to be physically appropriate, although they are not unique. They should not deviate from the actual helical patterns too far.
- The modeled bulk Lorentz factor and Doppler factor derived for the superluminal components by model-fits of their kinematics clearly revealed the acceleration/deceleration in their motion. These anticipatively-derived Doppler factors provide valuable opportunities to study the relation between their flux-evolution and the Doppler-boosting effect: a key test for our precessing nozzle scenario.
- The flare events (flux variations) observed to occur in their inner trajectory-sections for all the five superluminal components (C4, C5, C9, C10 and C22) could be fully interpreted in terms of their Doppler-boosting effects. The kinematics, dynamics and emission properties of all the five superluminal components were consistently well interpreted, thus validating the whole scenario and the model-simulation methods. [7]

References

Artymovicz P., 1998, in: Theory of Black Hole Accretion Disks, ed. M.A. Abramowicz, G. Björnsson, J.E. Pringle, p202

Babadzhantants M.K., Belokon E.T. & Gamm N.G., 1995, Astronomy Report 39, 393

Begelman M.C., Blandford R.D. & Rees M.J., 1980, Nature 287, 307

Biretta J.A., Moore R.L. & Cohen M.H., 1986, ApJ 308,93

Blandford R.D., Znajek R.I., 1977, MNRAS 179, 433

Blandford R.D., Payne D.G., 1982, MNRAS 199, 883

Britzen S., Qian S.J., Steffen W., et al., 2017, A&A 602A, 29

Camenzind M., 1986, A&A 162, 32

Camenzind M., 1987, A&A 184, 341

Camenzind M., 1990, Reviews in Modern Astronomy 3, p234

Hardee P.E., 1987, ApJ 318, 78

Homan D.C., Lister M.L., Kovalev Y.Y., et al. 2014, ApJ 798 , 134

Hogg D.W., 1999, astro-ph/9905116

Jorstad S.G., Marscher A.P., Lister M.L., et al., 2005, AJ 130, 1418

Jorstad S.G., Marscher A.P., Smith P.S., et al. 2013, ApJ 773, 147

Jorstad S.G., Marscher A.P., Morozova D.A., et al., 2017, ApJ 846, article id. 98

Klare J., 2003, Quasi-Periodicity in the Parsec-Scale Jet of the Quasar 3C345, PhD Thesis, Rheinische-Friedrich-Wilhelms-Universität Bonn, Bonn, Germany

Klare J., Zensus J.A., Lobanov A.P., et al., 2005, in "Future Directions in High Resolution astronomy: The 10th Anniversary of the VLBA", ASP Conference Series, Vol.340 (eds. J.D. Romney and M.J. Reid), p.40

Kudryavtseva N.A. & Pyatunina T.B., 2006, Astronomy Report 50, 1

Li Z.Y., Chiueh T., Begelman M.C., 1992, ApJ 394, 459

Lobanov A.P. & Roland J., 2005, A&A 431, 831

Lobanov A.P., Zensus J.A., 1999, ApJ 521, 509

Lovelace R.V.E., Mehanian C., Mobarry C.M., Sulkanen M.E., 1986, ApJS 62, 1

Meier D.L. & Nakamura M., 2006, in: Blazar Variability Workshop II: Entering the GLAST Era, ed. H.R. Miller, K. Marshall, J.R. Webb & M.F. Aller, ASP Conf. Ser., 350, 195

Nakamura M. & Asada K., 2013, ApJ 775, 118

Qian S.J., Witzel A., Krichbaum T., et al., 1991a, Acta Astron. Sin. 32, 369 (Chinese Astro. Astrophys. 16, 137 (1992))

Qian S.J., Krichbaum T.P., Witzel A., et al., 1991b, in: High Energy/Astrophysics: Compact Stars and Active Galaxies (Proceedings of the 3rd Chinese Academy of Sciences and Max-Planck Society workshop held 19-23, October 1990 in Huangshan, China. Edited by Qibin Li, Singapore: World Scientific), p.80

Qian S.J., & Zhang X.Z., 1999, Acta Astrophysica Sinica 19, 128

Qian S.J., Kudryavtzva N.A., Britzen S., et al., 2007, Chin. J. Astrophys. 7, 364

Qian S.J., Witzel A., Zensus J.A., et al., 2009, Research in Astron. Astrophys. 9, 137

Qian S.J., Krichbaum T.P., Zensus J.A., et al., 1996, A&A 308, 395

Qian S.J., 2013, Research in Astron. Astrophys. 13, 783

Qian S.J., Britzen S., Witzel A., et al. 2014, Research in Astron. Astrophys. 14, 249

Qian S.J., 2016, Res. in Astron. Astrophys. 16, 20

Qian S.J., Britzen S., Witzel A., et al., 2017, A&A 604, A90

Qian S.J., Britzen S., Witzel A., et al., 2018a, A&A 615, A123

Qian S.J., 2018b, arXiv:1811.11514

Qian S.J., Britzen S., Krichbaum T.P., Witze A., 2019a, A&A 621, A11

Qian S.J., 2019b, arXiv:1904.03357

Qian S.J., 2019c, arXiv:1906.09782

Qian S.J., 2020, arXiv:2005.05517

Qian S.J., Britzen S., Krichbaum T.P., Witzel A., 2021, A&A 653, A7

Qian S.J., 2022, arXiv:2022.01915

Roland J., Britzen S., Caproni A., et al., 2013, A&A 557, 85

Schinzel F.K., Lobanov A.P., Zensus J.A., 2010, in: "Accretion and Ejection in AGNs: A Global View", ASP Conference series, Vol. 427, eds. L. Maraschi, G.Ghisellini, R. Della Ceca and F. Tavecchio, p153

Schinzel F.K., 2011a, Phyiscs and Kinematics of the Parsec Scale Jet of the Quasar 3C345, PhD Thesis, Universität zu Köln, Germany.

Schinzel F.K., Sokolovsky K.V., D'Ammando F., et al., 2011b, A&A 532, A150

Schinzel F.K., Lobanov A.P., Taylor G.B., et al., 2012a, A&A 537, A70

Schinzel F.K., Lobanov A.P., Zensus J.A., 2012b, Journal of Physics: Conference Series 372, 012070

Shi J.M., Kronik J.H., Lubow S.H., Hawley J.F., 2012, ApJ 749, 118

Shi J.M. & Krolik J.H., 2015, ApJ 807, article id.131

Sillanpää A., Haarala S.,Valtonen M.J., et al., 1988, ApJ 325, 628

Spergel D.N., Verde L., Peilis H.V., et al., 2003, ApJS 148, 145

Steffen W., Zensus J.A., Krichbaum T.P., et al., 1996, A&A 302, 335.

Unwin S.C., Wehrle A.E., Lobanov A.P., et al., 1997, ApJ 480, 596

[6] Possible evidence of a double-jet structure has been discussed in Qian (2022). The close relation between the flux evolution and Doppler-boosting effect for the superluminal components in jet-B of 3C345 (in addition to jet-A) will be presented elsewhere, further justifying the double-nozzle structure in 3C345.

[7] The shorter time-scale flux variations had no relation to the Doppler-boosting effect induced by the intrinsic acceleration/deceleration of the knots could be due to the variations in the intrinsic flux density and spectral index of the knots at different frequencies (Equation (22) in Sect.4).

Villata M., Raiteri C., Sillanpää A., Takalo L.O., 1998, MNRAS 293, L13
Vlahakis N. & Königl A., 2003, ApJ 596, 1080
Vlahakis N. & Koenigl A., 2004, ApJ 605, 656
Wang J.M., Luo B., Ho L.C., 2004, ApJ 615, L9
Willis A.G., et al., 1974, Nature 250, 625
Zensus, J.A., 1997, ARA&A 35, 607

Appendix A: Doppler boosting effect and flux evolution of a superluminal component in blazar 3C279

3C279 is one of the most prominent blazars which have been intensively observed and studied on VLBI-scales. The VLBI-kinematic behaviors observed at 43 GHz of its superluminal components have been analyzed in detail and successfully interpreted and model-simulated in terms of the precessing nozzle scenario with a double-jet structure for 31 components (Qian et al. 2019a).

Here as a supplement, we introduce the results of model-fitting of the VLBI-kinematics for one superluminal component C13 in 3C279 and the interpretation of its flux evolution in terms of its Doppler-boosting effect during its accelerated and decelerated motion.

In the previous paper (Qian et al. 2019a) the superluminal components in 3C279 was assumed to move along a common parabolic trajectory which precesses to give rise to the individual trajectories of the knots at their corresponding precession phases. In this framework, knot C13 had its ejection time t_0=1998.88 and corresponding precession phase ω=3.65 rad. Its bulk Lorentz factor $\Gamma(t)$ and Doppler factor $\delta(t)$ were derived as functions of time, showing its accelerated motion during the period 1999.2–1999.5. Its modeled Lorentz factor and Doppler factor increased. The anticipatively-derived Doppler factor implied that knot C13 should have flux variations induced by the Doppler boosting effect. However, in the previous model-simulation of the kinematics for knot C13 we did not take its deceleration after ∼1999.5 into consideration.

Here in this appendix, for analyzing the relation between its flux evolution and Doppler boosting effect during the period ∼1999.0-2001.0, we take both its accelerated and decelerated motion into consideration in order to fit the rising and decaying phases of its 15 GHz flux light curve. The 15GHz flux density data was adopted from Roland et al. (2013), where the knot was designated as C5.

In Figure A.1 are shown the travelled distance Z(t) along the Z-axis (top panel), the curves of parameters $\epsilon(t)$ and $\psi(t)$, and the model-fit of the inner trajectory-section ($X_n \leq 0.1$ mas).

The curves of ϵ and ψ (middle panel of Fig.A.1) show that ϵ=1.32°=constant, but parameter ψ changed with time: before 1999.25 (Z≤5.02 mas, $r_n \leq 0.15$ mas and $X_n \leq 0.10$ mas,) ψ=28.70°, and after 1999.25 ψ increased to 34.38° at 1999.37 (Z=7.0 mas). Thus knot C13 moved along the precessing common trajectory within $X_n \leq 0.10$ mas and its precessing common trajectory section extended to ∼33.4 pc. Beyond X_n=0.10 mas it moved along its own individual trajectory in its outer trajectory section.

In the bottom panel of Fig.A.1 the model-fit to its inner trajectory section is shown, where knot C13 moved along the precessing common trajectory: the dashed lines in black, magneta and blue represent the precessing common trajectories corresponding to the precession phases ω=3.65 rad and 3.65±0.63 rad (±10% of the preecssion period), respectively.

The model-fits to its kinematics are shown in Figure A.2, including its whole trajectory $Z_n(X_n)$, core separation $r_n(t)$ and coordinate $X_n(t)$ (upper three panels), and coordinate $Z_n(t)$, the derived apparent-speed $\beta_{app}(t)$/viewing-angle $\theta(t)$ and the derived Lorentz-factor $\Gamma(t)$ and Doppler-factor $\delta(t)$ are shown in the bottom three panels. Specifically, its

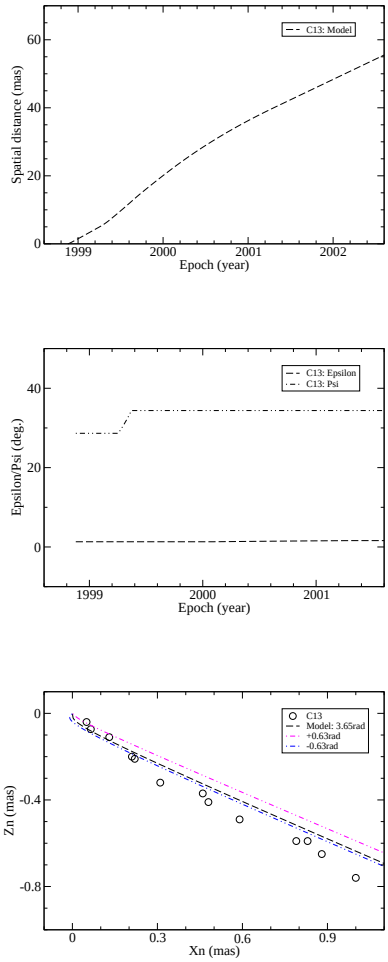


Fig. A.1. Knot C13 in 3C279. Top panel: the travelled distance Z(t) along the Z-axis. The curves of $\epsilon(t)$ and $\Psi(t)$ (middle panel) shows that for Z>5.0 mas (or after 1999.25) parameter ψ started to increase and knot C13 started to move along its own individual trajectory. The model fit to its inner trajectory section ($X_n \leq 0.10$ mas, $t \leq 1999.25$) in terms of the precessing common trajectory is shown in the bottom panel: the curves in black, magenta and blue represent the precessing common trajectories for the precession phases ω=3.65 rad and 3.65±0.63 rad (±10% of the precession period), respectively.

bulk Lorentz factor was modeled as: for Z≤5.0 mas Γ=16.0; for Z=5.0-13.0 mas Γ increased from 16.0 t0 21.0 (maximum Lorentz factor at 1999.65); for Z=13.0-40.0 mas Γ decreased from 21.0 t0 15.0 and then kept to be constant. Correspondingly, the Doppler factor had similar variations with a maximum value δ_{max}=33.68 at Z=13.0 mas (t=1999.65). During the period 1999.25-2001.0 the derived apparent speed had a bump structure similar to that of Lorentz/Doppler factor, but the derived viewing angle changed in a very small range [1.39°-1.34°-1.56°].
Obviously, the bump structure of its Doppler factor as a function of time which was anticipatively-determined for knot C13 indicated the existence of Doppler boosting effect in its flux evolution. Using the derived Doppler factor $\delta(t)$ and arbitrarily assuming a spectral index α=0.5, we performed the model-fits to the observed 15 GHz light curves (one for the observed flux density light-curve and the other for the normalized flux light curve) in Figure A.3. It can be seen that both the flux light-curves were very well coincident with its Doppler boosting profile. Thus we see that the kinematic behavior and the emission properties observed for superluminal component C13 in 3C279 could be consistently and successfully interpreted in terms of our precessing jet-nozzle scenario (Qian et al. 2019a).

We have made detailed studies of the close relation between Doppler-boosting effect and flux evolution for the superluminal components in 3C345 and 3C279, and shown that their kinematic/dynamic behaviors and emission properties can consistently and successfully interpreted in terms of our precessing nozzle scenario. Thus the investigation of the relation between Doppler-boosting effect and flux evolution for the superluminal components in other blazars or AGNs (e.g., 3C454.3, OJ287 and B1308+326) would be important. We would like to try to do some work in the near future.

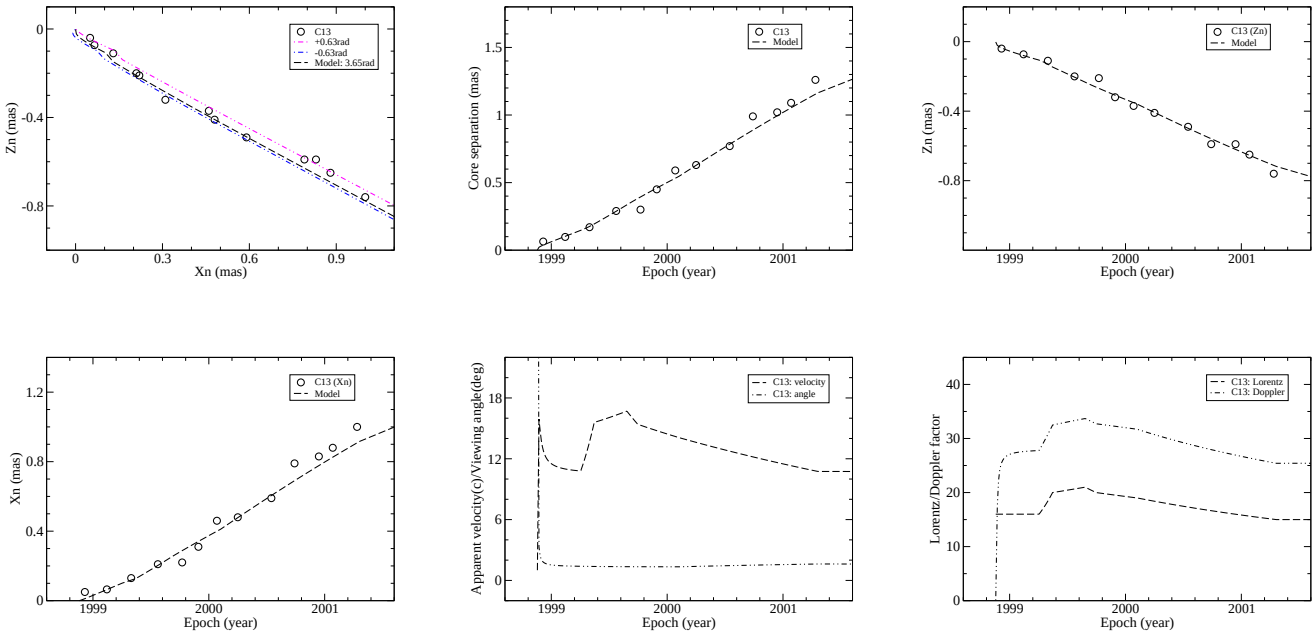


Fig. A.2. Knot C13 in 3C279: Model-fits to the whole kinematics,including both inner trajectory-section (within $r_n \leq 0.15$ mas, where knot C13 moved along the precessing common trajectory) and outer trajectory section (beyond $r_n = 0.15$ mas, where knot C13 moved along its own individual trajectory): the whole trajectory, core separation and coordinate X_n (top three panels); coordinate Z_n, apparent-velocity/viewing-angle and bulk Lorentz-factor/Doppler-factor (bottom three panels).

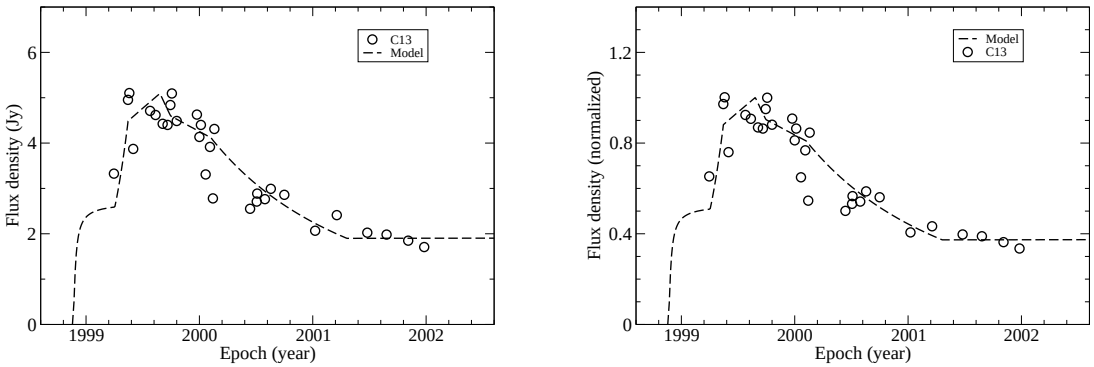


Fig. A.3. Knot C13 in 3C279: The observed 15 GHz light curve (left panel) and the normalized flux light curve are well interpreted in terms of its Doppler boosting effect ($\propto [\delta(t)/\delta_{max}]^{3.5}$).